Research Paper
Computational Methods for Differential Equations
http://cmde.tabrizu.ac.ir
Vol. *, No. *, *, pp. 1-31
DOI:10.22034/cmde.2026.70406.3498

Exploration of nonlinear soliton dynamics, bifurcation, and chaos of the coupled Klein-Gordon-Zakharov system

Tobibur Rahman[1], **Md. Tarikul Islam**[1], **and M. Ali Akbar**[2,3,*]

[1]Department of Mathematics, Hajee Mohammad Danesh Science and Technology University, Dinajpur, Bangladesh.

[2]Miyan Research Institute, International University of Business Agriculture and Technology, Dhaka, Bangladesh.

[3]Department of Applied Mathematics, University of Rajshahi, Bangladesh.

Abstract

In this article, we investigate the nonlinear dynamical behavior of the coupled Klein-Gordon-Zakharov system, which models the interaction between high-frequency electric field oscillations and low-frequency ion-acoustic waves in plasma. Employing the improved auxiliary equation approach and the improved tanh method, a diverse range of exact soliton solutions, including localized W-shaped, singular, rational, bell-shaped, kink, and periodic waveforms, is constructed, each describing different modes of nonlinear wave propagation. The qualitative features of these solutions are analyzed through contour, two- and three-dimensional graphical representations, emphasizing the impact of parameter variations, particularly the wave speed, on amplitude, localization, and wave stability. Also, the accuracy of the derived exact wave solutions is successfully validated through independent numerical simulations using the finite difference method. A detailed bifurcation analysis based on planar dynamical systems theory is carried out to reveal multiple equilibrium configurations, such as centers and saddles, related to the transition between stable and unstable states. Furthermore, the formation of quasi-periodic and chaotic orbitals under external perturbations is demonstrated, indicating the nonlinear sensitivity of the system. Additionally, the modulation instability criteria are formulated to assess the stability of the steady-state regimes, and these theoretical conditions are computationally verified by perturbing the exact soliton. The results provide a detailed physical understanding of nonlinear plasma wave interactions, contributing to the development of advanced models for high-energy plasma wave modulation, energy transport, and controlled wave propagation.

Keywords. Exact soliton solutions, Modulation instability, Finite difference method, Bifurcation and chaos, Improved auxiliary equation and improved tanh methods.

2010 Mathematics Subject Classification. 65L05, 34K06, 34K28.

1. Introduction

Nonlinear differential equations (NLDEs) play a dynamic role in describing complex phenomena observed in various real-world systems. Many real-world problems in diverse scientific domains such as solid-state physics, optics, bioinformatics, plasma physics, finance, biological sciences, applied mathematics, signal processing, mechanics and chemical kinetics are effectively modeled using nonlinear partial differential equations (NLPDEs) [7, 9, 39]. Theoretical and experimental investigations of these models have attracted substantial research interest in recent years. Recent advances in qualitative theory of dynamical systems and exact solution methodologies have further enhanced the analytical framework for characterizing various complex nonlinear models, including optical pulse propagation and plasma dynamics [8, 22, 31, 37, 41, 47, 48]. Therefore, several computational and analytical techniques have been developed to obtain accurate and efficient wave solutions for NLPDEs, which has advanced the understanding of nonlinear dynamical behavior in multiple disciplines.

Received: 26 November 2025; Accepted: 01 September 2026.
* Corresponding author. Email: ali_math74@yahoo.com.

Thus, analytical methods widely applied to derive exact solutions for nonlinear evolution equations include the improved auxiliary equation method [15], Hirota bilinear scheme [13], inverse scattering transform approach [2], sine-cosine method [40], rational (G'/G)-expansion approach [16], Jacobi elliptic function expansion technique [25], extended exp-function process [34], improved tanh scheme [17], Sardar sub-equation approach [32], mapping method [29], Darboux transformation scheme [26], rational $(1/\phi')$-expansion technique [18], generalized Kudryashov scheme [10], sine-Gordon expansion approach [43], Painlevé analysis [23], enhanced rational (G'/G)-expansion scheme [19], unified technique [1], among others. Despite these developments, formulating more robust, flexible, and unifying mathematical approaches remains a primary focus in contemporary physical research.

The coupled Klein-Gordon-Zakharov (cKGZ) system is an important nonlinear mathematical model that describes the interaction between low-frequency ion-acoustic waves in plasma and high-frequency electric field oscillations. It combines the properties of the Klein-Gordon equation, which governs the evolution of fast-varying high-frequency fields, with the Zakharov equation, which represents the slow dynamics of plasma density fluctuations. The cKGZ system is expressed as coupled nonlinear equations that model the mutual pairing between the envelope of an electrostatic wave and the ion density perturbation, which is as follows [14]:

$$\Xi_{tt} - \Xi_{xx} + \Xi + a\Xi\Pi = 0, \tag{1.1}$$

$$\Pi_{tt} - \Pi_{xx} - b(|\Xi|^2)_{xx} = 0, \tag{1.2}$$

where $\Xi(x,t)$ and $\Pi(x,t)$ are complex-valued and real-valued functions, respectively; t stands for time and x represents space in the path of wave propagation, while a and b are non-zero free constants. The coupling captures key physical processes such as wave modulation, self-interaction, and energy exchange between fast and slow plasma modes. The cKGZ model has been investigated through some analytical and numerical techniques. For example, exact solutions have been derived through expansion frameworks, including the extended rational sine-cosine and extended rational sinh-cosh techniques [14, 42], the $\exp(-\phi(\xi))$-expansion scheme [11], the extended direct algebraic approach [30] and the extended sinh-Gordon equation approach [6]. Hyperbolic and trigonometric function approaches, including the extended tanh [3], the sine-cosine [36], and extended hyperbolic approaches [35], are employed to extract wave solutions. Other analytical formulations include the generalized Khater method [20], the solitary wave ansatz [38], and the simplest equation method [27]. In addition to analytical studies, semi-analytical solutions have been constructed using techniques like the Adomian decomposition and B-spline method [21]. Moreover, recent studies have explored the bifurcations, dynamic behaviors [45], and orbital stability [12, 24, 44, 46] of the travelling wave solutions for this stated nonlinear system.

Although the cKGZ system has been previously studied for nonlinear wave interactions, existing literature predominantly focuses on deriving analytic or numerical solutions. Most of these studies emphasize only the construction of exact soliton solutions without exploring their dynamic stability, bifurcation characteristics, and chaotic behaviors in detail. Furthermore, the impact of system parameters on wave profiles, amplitude modulation, and transitions between stable and unstable regimes remains largely unaddressed from the perspective of dynamical systems theory. The absence of a unified framework combining analytical derivation, bifurcation structure, and chaotic evolution limits the comprehensive understanding of nonlinear wave propagation and energy exchange mechanisms.

Hence, a detailed analytical and qualitative study is required to bridge the gap between exact wave solutions and their physical stability characteristics. Therefore, the objective of this study is to conduct an analytical and dynamical investigation of the nonlinear cKGZ system by utilizing the improved auxiliary equation and improved tanh methods to derive a broad class of exact soliton solutions. The novelty of this research lies in the integrated analysis; in comparison to classical approaches that often yield a restricted solution set, the suggested methods systematically extract a broader class of exact solutions, including localized W-shaped solitons, singular, periodic, kink, dark, bright, and rational waves, within a single mathematical framework. In addition to constructing these solutions, this study explores the qualitative dynamics of the system through bifurcation, phase plane, potential energy, and chaos analyses, highlighting the sensitivity of wave behavior to parameter variations. This is further supplemented by verifications of modulation instability. This integrated approach provides both theoretical and practical insights into the control and prediction of nonlinear wave phenomena in related physical systems. Table 1 presents a comparative analysis between the proposed methodology and existing literature, highlighting the key contributions of this article.

Table 1. Comparison between the suggested methodology and existing literature for the cKGZ system.

Key Features	Existing Literature [36]	Present Work
Methodology	Classical tanh, sine-cosine, exp-expansion	Improved auxiliary equation and improved tanh
Wave Solutions	Limited (solitary/periodic)	Diverse (W-shaped, singular, rational, periodic, kink, bright, dark, bell)
Qualitative Dynamics	Rarely explored; chaotic behavior absent	Comprehensive (bifurcation, phase portraits, chaos)
Stability & Validation	Mathematically unverified	Modulation instability & FDM validation
Wave Speed Influence	Unaddressed or restricted to static parameters	Analyzed via 2D projections across varying values of c
External Perturbation	Absent (focused solely on autonomous systems)	Included to investigate quasi-periodic and chaotic behaviors
Framework Integration	Fragmented (isolated analytical or numerical studies)	Unified (combining exact solutions, bifurcation, chaos, and FDM)

The arrangement of this article is organized as follows: Section 2 disclosures the improved auxiliary equation and improved tanh tools. Section 3 applies the mentioned methods to unravel the coupled Klein-Gordon-Zakharov model. Section 4 provides physical interpretations and graphical representations of the solutions. Section 5 presents the numerical simulation and verification to computationally establish the accuracy of the derived exact solutions. Section 6 offers a thorough analysis of bifurcation, phase plane analysis, sensitivity analysis, potential energy function, and chaotic behavior. Section 7 investigates the modulation instability of Eq. (1.1) and Eq. (1.2), which is further validated through a computational stability verification. Finally, the study is summarized in Section 8. The roadmap of the study is illustrated in Figure 1.

2. Outlines of technique

In this study, the nonlinear evolution equation with independent variables x and t is considered as follows:

$$A(P, P_x, P_t, \dots, P_{xx}, P_{tt}, P_{xt}, P_{xxx}, \dots) = 0, \tag{2.1}$$

where A is the function of the dependent variable P and its various partial derivatives. The wave variable $P = P(\sigma)$, $\sigma = \sigma(x, t, \dots)$ turns equation (2.1) into an ordinary differential equation with independent variable σ as follows:

$$B(P, P', P'', P''', \dots) = 0, \tag{2.2}$$

where B stands for a polynomial of P and its several ordinary derivatives with respect to a single independent variable σ. Eq. (2.2) is integrated one or more times if possible. The essential relations of the instructed schemes are given below:

2.1. The improved auxiliary equation scheme.

In line with the improved auxiliary equation scheme, the shape of the wave solution is stated as:

$$P(\sigma) = \frac{\sum_{i=0}^{m} g_i \rho^{i\psi(\sigma)}}{\sum_{i=0}^{m} h_i \rho^{i\psi(\sigma)}}, \tag{2.3}$$

where the unknown arbitrary parameters involved are evaluated with the help of some operations. The homogenous balance procedure serves the value of m, and $\rho^{\psi(\sigma)}$ satisfies the subsequent equation:

$$\psi'(\sigma) = \frac{1}{\ln \rho} \left\{ u\rho^{-\psi(\sigma)} + v + w\rho^{\psi(\sigma)} \right\}. \tag{2.4}$$

Eq. (2.4) ensures several solutions which are documented in [11]. The technique goes through some steps for exploring solutions of NLPDEs available in the aforementioned study [11].

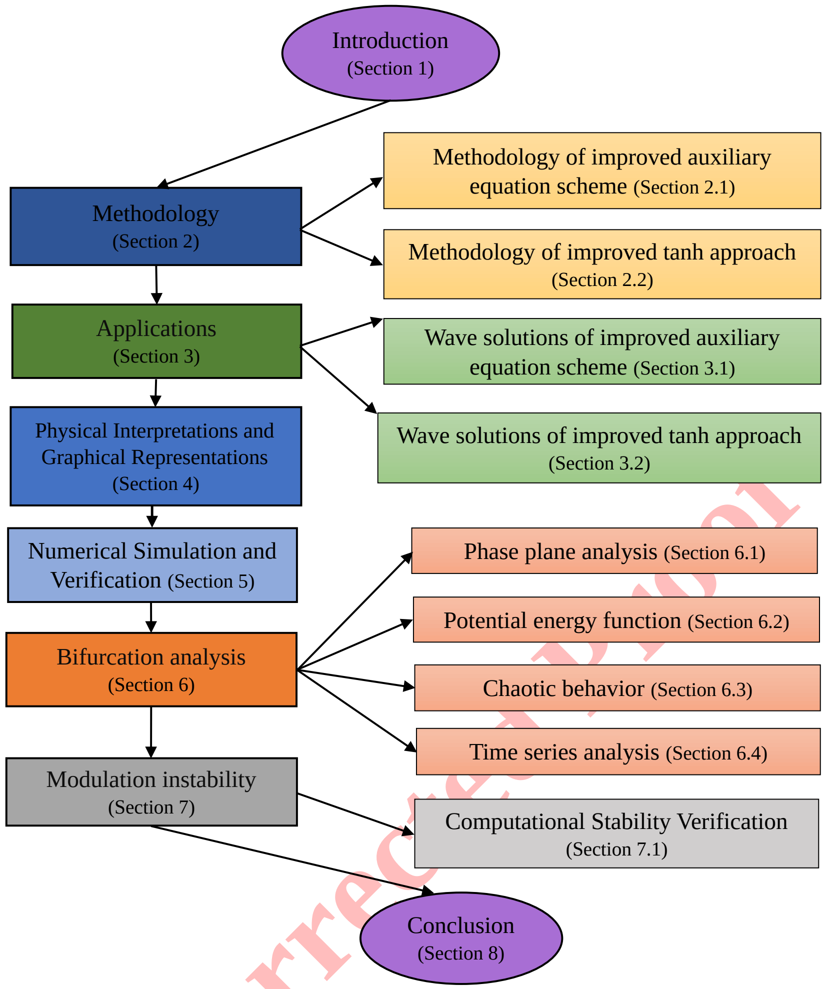

Figure 1. Flow chart of this study.

2.2. **The improved tanh approach.** This capable tool defines the wave solution as:

$$P(\sigma)=\frac{e_0+\sum_{i=1}^{m}\left(e_iH^i(\sigma)+f_iH^{-i}(\sigma)\right)}{g_0+\sum_{i=1}^{m}\left(g_iH^i(\sigma)+h_iH^{-i}(\sigma)\right)}, \tag{2.5}$$

whose unknown constants are determined hereafter. The value of m is evaluated by applying the homogeneous theme. The function $H=H(\sigma)$ satisfies:

$$H'(\sigma)=\phi+H^2(\sigma), \tag{2.6}$$

where ϕ is an arbitrary parameter. Eq. (2.6) ensures some solutions, which are documented in Ref. [18]. The main procedure of the improved tanh method has been conversed in Ref. [18].

Advantages of the utilized methods. The analytical techniques employed in this study, namely the improved auxiliary equation method and the improved tanh scheme, present several advantages for solving NLPDEs. Both approaches provide a systematic algebraic procedure to transform coupled PDEs into a system of algebraic equations. This formulation reduces computational overhead and is compatible with symbolic computation software. Furthermore, compared to classical techniques, these improved methods offer enhanced flexibility. They generate a broad spectrum of exact closed-form solutions, such as localized W-shaped solitons, singular, periodic, kink, antikink, bell, dark, bright, and rational wave structures, within a single mathematical framework by varying the physical parameters. The derived exact mathematical solutions facilitate physical interpretations, analysis of asymptotic wave behaviors, and dynamic evaluations, including the modulation instability and numerical verifications demonstrated in this study.

3. The wave solutions

The assumption. Let us consider the complex travelling wave transformation

$$\Xi(x,t) = p(x,t) + iq(x,t), \tag{3.1}$$

where $p(x,t)$ and $q(x,t)$ are real-valued functions. This yields the results

$$|\Xi|^2 = p^2 + q^2, \quad \Xi_{xx} = p_{xx} + iq_{xx}, \quad \Xi_{tt} = p_{tt} + iq_{tt}. \tag{3.2}$$

Utilizing Eqs. (3.1) and (3.2), substituting into Eqs. (1.1) and (1.2), we obtain

$$p_{tt} + iq_{tt} - (p_{xx} + iq_{xx}) + (p + iq) + a\Pi(p + iq) = 0, \tag{3.3}$$

$$\Pi_{tt} - \Pi_{xx} - b(p^2 + q^2)_{xx} = 0. \tag{3.4}$$

Separating the real and imaginary components of Eq. (3.3), we get

$$p_{tt} - p_{xx} + p + ap\Pi = 0, \tag{3.5}$$

$$q_{tt} - q_{xx} + q + aq\Pi = 0. \tag{3.6}$$

Assuming $p(x,t) = q(x,t)$, then Eqs. (3.4)–(3.6) reduce to

$$p_{tt} - p_{xx} + p + ap\Pi = 0, \tag{3.7}$$

$$\Pi_{tt} - \Pi_{xx} - 2b(p^2)_{xx} = 0. \tag{3.8}$$

We introduce the wave variables

$$p(x,t) = P(\sigma), \quad \Pi(x,t) = \Lambda(\sigma), \quad \text{where} \quad \sigma = k(x - ct), \tag{3.9}$$

where k and c represent the wave number and velocity, respectively. Applying these variables to Eqs. (3.7) and (3.8), we obtain

$$k^2(c^2 - 1)P'' + P + aP\Lambda = 0, \tag{3.10}$$

$$k^2(c^2 - 1)\Lambda'' - 2bk^2(P^2)'' = 0. \tag{3.11}$$

From Eq. (3.10), we find

$$\Lambda(\sigma) = \frac{k^2(1 - c^2)P''}{aP} - \frac{1}{a}. \tag{3.12}$$

Integrating Eq. (3.11) twice with respect to σ and setting the constants of integration to zero, we find

$$\Lambda(\sigma) = r + \frac{2bP^2}{c^2 - 1}, \tag{3.13}$$

where r stands for the constant of integration. Equating Eq. (3.12) and Eq. (3.13), we obtain

$$P'' + \frac{(1 + ar)}{k^2(c - 1)}P + \frac{2ab}{k^2(c - 1)^2}P^3 = 0. \tag{3.14}$$

By the homogeneous balance principle, balancing the highest order derivative term P'' and the nonlinear term P^3 gives $m = 1$. Based on this result, we proceed to construct wave solutions in the next section.

3.1. **The improved auxiliary equation scheme.** For $m = 1$, this method proposes the subsequent expression for the wave solution:

$$P(\sigma) = \frac{g_0 + g_1\rho^{\psi(\sigma)}}{h_0 + h_1\rho^{\psi(\sigma)}}, \tag{3.15}$$

where g_1 and h_1 are not equal to zero simultaneously, and the included parameters are evaluated accordingly. Inserting Eq. (2.4) and Eq. (3.15) into Eq. (3.14), we observe a polynomial in $\rho^{\psi(\sigma)}$. A system of algebraic equations is produced after assigning each coefficient of the polynomial to zero. The ensuing parameter values are found by solving the system of equations with the help of Maple software. To rationalize the mathematical content and maintain the analytical flow of the paper, we focus on the most representative parameter set (Case I) below. The redundant algebraic constraints for the other families (Case II and Case III) have been moved to Appendix A.

Case I:

$$g_0 = \pm\frac{(ar+1)(2uh_1 - vh_0)}{k(4uw - v^2)\sqrt{-ab}}, \quad g_1 = \pm\frac{(ar+1)(vh_1 - 2wh_0)}{k(4uw - v^2)\sqrt{-ab}},$$
$$c = \mp\frac{\sqrt{k^2(4uw - v^2) - 2(ar+1)}}{k\sqrt{4uw - v^2}}.$$

These sets of values are inserted into solution (3.15) with the solutions of Eq. (2.4), and therefore illustrious analytic solutions of the considered model are established. Accordingly, the general wave solutions for this representative case are:

$$P(\sigma) = \pm\frac{ar+1}{k(4uw - v^2)\sqrt{-ab}}\left(\frac{2uh_1 - vh_0 + (vh_1 - 2wh_0)\rho^{\psi(\sigma)}}{h_0 + h_1\rho^{\psi(\sigma)}}\right), \tag{3.16}$$

$$\Lambda(\sigma) = r + \frac{ar+1}{a(4uw - v^2)}\left(\frac{2uh_1 - vh_0 + (vh_1 - 2wh_0)\rho^{\psi(\sigma)}}{h_0 + h_1\rho^{\psi(\sigma)}}\right)^2, \tag{3.17}$$

where $\sigma = k\left(x \pm \frac{\sqrt{k^2(4uw-v^2)-2(ar+1)}}{k\sqrt{4uw-v^2}}t\right)$.

Under the conditions $v^2 - 4uw < 0$ and $w \neq 0$, we found the solutions as:

$$\Xi_1(\sigma) = \pm\frac{(1+i)(ar+1)}{k(4uw - v^2)\sqrt{-ab}}\left(\frac{h_1(v^2 - 4uw) - (vh_1 - 2wh_0)\sqrt{4uw - v^2}\tan\left(\frac{\sqrt{4uw-v^2}}{2}\sigma\right)}{h_1\left(v - \sqrt{4uw - v^2}\tan\left(\frac{\sqrt{4uw-v^2}}{2}\sigma\right)\right) - 2wh_0}\right), \tag{3.18}$$

$$\Pi_1(\sigma) = r + \frac{ar+1}{a(4uw - v^2)}\left(\frac{h_1(v^2 - 4uw) - (vh_1 - 2wh_0)\sqrt{4uw - v^2}\tan\left(\frac{\sqrt{4uw-v^2}}{2}\sigma\right)}{h_1\left(v - \sqrt{4uw - v^2}\tan\left(\frac{\sqrt{4uw-v^2}}{2}\sigma\right)\right) - 2wh_0}\right)^2, \tag{3.19}$$

$$\Xi_2(\sigma) = \pm\frac{(1+i)(ar+1)}{k(4uw - v^2)\sqrt{-ab}}\left(\frac{h_1(v^2 - 4uw) + (vh_1 - 2wh_0)\sqrt{4uw - v^2}\cot\left(\frac{\sqrt{4uw-v^2}}{2}\sigma\right)}{h_1\left(v + \sqrt{4uw - v^2}\cot\left(\frac{\sqrt{4uw-v^2}}{2}\sigma\right)\right) - 2wh_0}\right), \tag{3.20}$$

$$\Pi_2(\sigma) = r + \frac{ar+1}{a(4uw - v^2)}\left(\frac{h_1(v^2 - 4uw) + (vh_1 - 2wh_0)\sqrt{4uw - v^2}\cot\left(\frac{\sqrt{4uw-v^2}}{2}\sigma\right)}{h_1\left(v + \sqrt{4uw - v^2}\cot\left(\frac{\sqrt{4uw-v^2}}{2}\sigma\right)\right) - 2wh_0}\right)^2, \tag{3.21}$$

where $\sigma = k\left(x \pm \frac{\sqrt{k^2(4uw-v^2)-2(ar+1)}}{k\sqrt{4uw-v^2}}t\right)$.

Due to the conditions $v^2+4u^2>0$, $w\neq 0$, and $w=-u$, the solutions are:

$$\Xi_7(\sigma)=\mp\frac{(1+i)(ar+1)}{k(v^2+4u^2)\sqrt{-ab}}\left(\frac{h_1(v^2+4u^2)+(vh_1+2uh_0)\sqrt{v^2+4u^2}\tanh\left(\frac{\sqrt{v^2+4u^2}}{2}\sigma\right)}{2uh_0+h_1\left(v+\sqrt{v^2+4u^2}\tanh\left(\frac{\sqrt{v^2+4u^2}}{2}\sigma\right)\right)}\right), \tag{3.22}$$

$$\Pi_7(\sigma)=r-\frac{ar+1}{a(v^2+4u^2)}\left(\frac{h_1(v^2+4u^2)+(vh_1+2uh_0)\sqrt{v^2+4u^2}\tanh\left(\frac{\sqrt{v^2+4u^2}}{2}\sigma\right)}{2uh_0+h_1\left(v+\sqrt{v^2+4u^2}\tanh\left(\frac{\sqrt{v^2+4u^2}}{2}\sigma\right)\right)}\right)^2, \tag{3.23}$$

$$\Xi_8(\sigma)=\mp\frac{(1+i)(ar+1)}{k(v^2+4u^2)\sqrt{-ab}}\left(\frac{h_1(v^2+4u^2)+(vh_1+2uh_0)\sqrt{v^2+4u^2}\coth\left(\frac{\sqrt{v^2+4u^2}}{2}\sigma\right)}{2uh_0+h_1\left(v+\sqrt{v^2+4u^2}\coth\left(\frac{\sqrt{v^2+4u^2}}{2}\sigma\right)\right)}\right), \tag{3.24}$$

$$\Pi_8(\sigma)=r-\frac{ar+1}{a(v^2+4u^2)}\left(\frac{h_1(v^2+4u^2)+(vh_1+2uh_0)\sqrt{v^2+4u^2}\coth\left(\frac{\sqrt{v^2+4u^2}}{2}\sigma\right)}{2uh_0+h_1\left(v+\sqrt{v^2+4u^2}\coth\left(\frac{\sqrt{v^2+4u^2}}{2}\sigma\right)\right)}\right)^2, \tag{3.25}$$

where $\sigma=k\left(x\mp\frac{\sqrt{k^2(4u^2+v^2)+2(ar+1)}}{k\sqrt{4u^2+v^2}}t\right)$.

For $v^2-4u^2>0$ and $w=u$, the wave solutions are:

$$\Xi_{11}(\sigma)=\mp\frac{(1+i)(ar+1)}{k(4u^2-v^2)\sqrt{-ab}}\left(\frac{h_1(4u^2-v^2)+(2uh_0-vh_1)\sqrt{v^2-4u^2}\tanh\left(\frac{\sqrt{v^2-4u^2}}{2}\sigma\right)}{2uh_0-h_1\left(v+\sqrt{v^2-4u^2}\tanh\left(\frac{\sqrt{v^2-4u^2}}{2}\sigma\right)\right)}\right), \tag{3.26}$$

$$\Pi_{11}(\sigma)=r+\frac{ar+1}{a(4u^2-v^2)}\left(\frac{h_1(4u^2-v^2)+(2uh_0-vh_1)\sqrt{v^2-4u^2}\tanh\left(\frac{\sqrt{v^2-4u^2}}{2}\sigma\right)}{h_1\left(v+\sqrt{v^2-4u^2}\tanh\left(\frac{\sqrt{v^2-4u^2}}{2}\sigma\right)\right)-2uh_0}\right)^2, \tag{3.27}$$

$$\Xi_{12}(\sigma)=\mp\frac{(1+i)(ar+1)}{k(4u^2-v^2)\sqrt{-ab}}\left(\frac{h_1(4u^2-v^2)+(2uh_0-vh_1)\sqrt{v^2-4u^2}\coth\left(\frac{\sqrt{v^2-4u^2}}{2}\sigma\right)}{h_1\left(v+\sqrt{v^2-4u^2}\coth\left(\frac{\sqrt{v^2-4u^2}}{2}\sigma\right)\right)-2uh_0}\right), \tag{3.28}$$

$$\Pi_{12}(\sigma)=r+\frac{ar+1}{a(4u^2-v^2)}\left(\frac{h_1(4u^2-v^2)+(2uh_0-vh_1)\sqrt{v^2-4u^2}\coth\left(\frac{\sqrt{v^2-4u^2}}{2}\sigma\right)}{h_1\left(v+\sqrt{v^2-4u^2}\coth\left(\frac{\sqrt{v^2-4u^2}}{2}\sigma\right)\right)-2uh_0}\right)^2, \tag{3.29}$$

where $\sigma=k\left(x\pm\frac{\sqrt{k^2(4u^2-v^2)-2(ar+1)}}{k\sqrt{4u^2-v^2}}t\right)$.

Under the conditions $v=w=M$ and $u=0$, we get the wave solutions:

$$\Xi_{18}(\sigma)=\mp\frac{(1+i)(ar+1)}{kM\sqrt{-ab}}\left(\frac{(h_0-h_1)e^{M\sigma}+h_0}{(h_0-h_1)e^{M\sigma}-h_0}\right), \tag{3.30}$$

$$\Pi_{18}(\sigma)=r-\frac{ar+1}{a}\left(\frac{(h_0-h_1)e^{M\sigma}+h_0}{(h_0-h_1)e^{M\sigma}-h_0}\right)^2, \tag{3.31}$$

where $\sigma=k\left(x\mp\frac{\sqrt{k^2M^2+2(ar+1)}}{kM}t\right)$.

For the assumption $u = 0$, we found the results as:

$$\Xi_{21}(\sigma) = \mp\frac{(1+i)(ar+1)}{kv\sqrt{-ab}}\left(\frac{(vh_1 - wh_0)e^{v\sigma} - h_0}{(vh_1 - wh_0)e^{v\sigma} + h_0}\right), \tag{3.32}$$

$$\Pi_{21}(\sigma) = r - \frac{ar+1}{a}\left(\frac{(vh_1 - wh_0)e^{v\sigma} - h_0}{(vh_1 - wh_0)e^{v\sigma} + h_0}\right)^2, \tag{3.33}$$

where $\sigma = k\left(x \mp \frac{\sqrt{k^2v^2+2(ar+1)}}{kv}t\right)$.

According to the conditions $w = 0$, we attain:

$$\Xi_{24}(\sigma) = \mp\frac{(1+i)(ar+1)}{kv^2\sqrt{-ab}}\left(\frac{vh_1(qe^{v\sigma} - p) + q(2uh_1 - vh_0)}{h_1(qe^{v\sigma} - p) + qh_0}\right), \tag{3.34}$$

$$\Pi_{24}(\sigma) = r - \frac{ar+1}{av^2}\left(\frac{vh_1(qe^{v\sigma} - p) + q(2uh_1 - vh_0)}{h_1(qe^{v\sigma} - p) + qh_0}\right)^2, \tag{3.35}$$

where $\sigma = k\left(x \mp \frac{\sqrt{k^2v^2+2(ar+1)}}{kv}t\right)$.

3.2. **The improved tanh technique.** This method defines the wave solutions as:

$$P(\sigma) = \frac{e_0 + e_1H(\sigma) + f_1H^{-1}(\sigma)}{g_0 + g_1H(\sigma) + h_1H^{-1}(\sigma)}. \tag{3.36}$$

Eq. (3.14) stands for a polynomial with the usage of the solution (3.36) and Eq. (2.6). Immediately, locate every term of the polynomial to zero and solve them by employing Maple to generate the succeeding outcomes. To focus on the illustrative wave dynamics and avoid mathematical redundancy, we select the first two cases to expose the ensuing solutions in the main text. The algebraic parameter sets for the remaining cases (Case III to Case VI) are comprehensively listed in Appendix A.

Case I:

$$e_0 = e_1 = 0, \quad f_1 = \pm\frac{g_0(ar+1)}{2k\sqrt{-ab}}, \quad g_1 = h_1 = 0, \quad \phi = -\frac{ar+1}{2k^2(c^2-1)}.$$

Case II:

$$e_0 = \mp\frac{kh_1(c^2-1)}{\sqrt{-ab}}, \quad e_1 = 0, \quad f_1 = \mp\frac{g_0(ar+1)}{2k\sqrt{-ab}}, \quad g_1 = 0, \quad \phi = -\frac{ar+1}{2k^2(c^2-1)}.$$

These determined values of free constants are added in Eq. (3.36) and taken together with the solutions of Eq. (2.6) to make sure analytic solutions are established. Exposing the ensuing solutions for these selected cases yields the following:

Solution Set 1: According to Case I

$$P_1(\sigma) = \mp\frac{ar+1}{2k\sqrt{-ab}H(\sigma)}, \tag{3.37}$$

$$\Lambda_1(\sigma) = r - \frac{(ar+1)^2}{2ak^2(c^2-1)H(\sigma)^2}, \tag{3.38}$$

where $\sigma = k(x - ct)$.

For $\phi < 0$, the generated solutions are:

$$\Xi_1^1(\sigma) = \pm\frac{(1+i)(ar+1)}{2k\sqrt{ab\phi}\tanh(\sqrt{-\phi}\sigma)}, \tag{3.39}$$

$$\Pi_1^1(\sigma) = r + \frac{(ar+1)^2}{2ak^2(c^2-1)\phi\tanh^2(\sqrt{-\phi}\sigma)}, \tag{3.40}$$

$$\Xi_1^2(\sigma) = \pm\frac{(1+i)(ar+1)}{2k\sqrt{ab\phi}\coth(\sqrt{-\phi}\sigma)}, \tag{3.41}$$

$$\Pi_1^2(\sigma) = r + \frac{(ar+1)^2}{2ak^2(c^2-1)\phi\coth^2(\sqrt{-\phi}\sigma)}, \tag{3.42}$$

where $\sigma = k(x-ct)$ and $\phi = -\frac{ar+1}{2k^2(c^2-1)}$.

Under the condition $\phi > 0$, the results obtained are:

$$\Xi_1^3(\sigma) = \mp\frac{(1+i)(ar+1)}{2k\sqrt{-ab\phi}\tan(\sqrt{\phi}\sigma)}, \tag{3.43}$$

$$\Pi_1^3(\sigma) = r - \frac{(ar+1)^2}{2ak^2(c^2-1)\phi\tan^2(\sqrt{\phi}\sigma)}, \tag{3.44}$$

$$\Xi_1^4(\sigma) = \pm\frac{(1+i)(ar+1)}{2k\sqrt{-ab\phi}\cot(\sqrt{\phi}\sigma)}, \tag{3.45}$$

$$\Pi_1^4(\sigma) = r - \frac{(ar+1)^2}{2ak^2(c^2-1)\phi\cot^2(\sqrt{\phi}\sigma)}, \tag{3.46}$$

where $\sigma = k(x-ct)$ and $\phi = -\frac{ar+1}{2k^2(c^2-1)}$.

Solution Set 2: Due to Case II

$$P_2(\sigma) = \mp\frac{g_0(ar+1)+2(c^2-1)k^2h_1H(\sigma)}{2k\sqrt{-ab}\{h_1+g_0H(\sigma)\}}, \tag{3.47}$$

$$\Lambda_2(\sigma) = r - \frac{\{g_0(ar+1)+2(c^2-1)k^2h_1H(\sigma)\}^2}{2ak^2(c^2-1)\{h_1+g_0H(\sigma)\}^2}, \tag{3.48}$$

where $\sigma = k(x-ct)$.

For $\phi < 0$, we attain the solutions:

$$\Xi_2^1(\sigma) = \pm\frac{(1+i)\{g_0(ar+1)-2(c^2-1)k^2h_1\sqrt{-\phi}\tanh(\sqrt{-\phi}\sigma)\}}{2k\sqrt{-ab}\{g_0\sqrt{-\phi}\tanh(\sqrt{-\phi}\sigma)-h_1\}}, \tag{3.49}$$

$$\Pi_2^1(\sigma) = r - \frac{\{g_0(ar+1)-2(c^2-1)k^2h_1\sqrt{-\phi}\tanh(\sqrt{-\phi}\sigma)\}^2}{2ak^2(c^2-1)\{g_0\sqrt{-\phi}\tanh(\sqrt{-\phi}\sigma)-h_1\}^2}, \tag{3.50}$$

$$\Xi_2^2(\sigma) = \pm\frac{(1+i)\{g_0(ar+1)-2(c^2-1)k^2h_1\sqrt{-\phi}\coth(\sqrt{-\phi}\sigma)\}}{2k\sqrt{-ab}\{g_0\sqrt{-\phi}\coth(\sqrt{-\phi}\sigma)-h_1\}}, \tag{3.51}$$

$$\Pi_2^2(\sigma) = r - \frac{\{g_0(ar+1)-2(c^2-1)k^2h_1\sqrt{-\phi}\coth(\sqrt{-\phi}\sigma)\}^2}{2ak^2(c^2-1)\{g_0\sqrt{-\phi}\coth(\sqrt{-\phi}\sigma)-h_1\}^2}, \tag{3.52}$$

where $\sigma = k(x-ct)$ and $\phi = -\frac{ar+1}{2k^2(c^2-1)}$.

For $\phi > 0$, we found the outcomes:

$$\Xi_2^3(\sigma) = \pm \frac{(1+i)\{g_0(ar+1) + 2(c^2-1)k^2 h_1 \sqrt{\phi}\tan(\sqrt{\phi}\sigma)\}}{2k\sqrt{-ab}\{g_0\sqrt{\phi}\tan(\sqrt{\phi}\sigma) + h_1\}}, \tag{3.53}$$

$$\Pi_2^3(\sigma) = r - \frac{\{g_0(ar+1) + 2(c^2-1)k^2 h_1 \sqrt{\phi}\tan(\sqrt{\phi}\sigma)\}^2}{2ak^2(c^2-1)\{g_0\sqrt{\phi}\tan(\sqrt{\phi}\sigma) + h_1\}^2}, \tag{3.54}$$

$$\Xi_2^4(\sigma) = \pm \frac{(1+i)\{g_0(ar+1) - 2(c^2-1)k^2 h_1 \sqrt{\phi}\cot(\sqrt{\phi}\sigma)\}}{2k\sqrt{-ab}\{g_0\sqrt{\phi}\cot(\sqrt{\phi}\sigma) - h_1\}}, \tag{3.55}$$

$$\Pi_2^4(\sigma) = r - \frac{\{g_0(ar+1) - 2(c^2-1)k^2 h_1 \sqrt{\phi}\cot(\sqrt{\phi}\sigma)\}^2}{2ak^2(c^2-1)\{g_0\sqrt{\phi}\cot(\sqrt{\phi}\sigma) - h_1\}^2}, \tag{3.56}$$

where $\sigma = k(x-ct)$ and $\phi = -\frac{ar+1}{2k^2(c^2-1)}$.

The above analytic solutions in exact form possess inordinate significance for describing the solitons in high-frequency plasma physics. The physical profiles of the furnished solutions have been depicted through 3D, 2D, and contour sketches to make the dynamic premise of nonlinear waves understandable. The accomplishments of the present effort due to generality and newness are worth declaring in comparison to references [27, 38].

4. Physical interpretations and graphical representations

Standard periodic waves are regular and repeating over time and space without such disruptions, with a uniform frequency. Bright solitons are localized regions of increased plasma density, corresponding to wave peaks, and anti-bell-shaped solitons are localized regions of lower plasma density, corresponding to wave troughs. Kink structures correspond to helical distortions in magnetic field lines; the energy of the magnetic field is transferred from the magnetic field to plasma particles, resulting in increased particle motion and localized heating. The anti-kink soliton is the opposite of this process. Also, the W-shaped soliton is the product of nonlinear dispersive effects that combine localized density peaks and troughs in one coherent wave structure. In plasma, singular periodic events represent illustrations when the regular periodicity of the plasma has been disrupted by one event, such as a shock or discontinuity, which can cause abrupt changes in the plasma parameters.

The graphical representations presented in Figures 2–10 illustrate the diverse physical profiles of the exact soliton solutions systematically derived via the improved auxiliary equation method. Figure 2 illustrates a singular periodic soliton corresponding to solution (3.18) using the parameters $a = h_1 = 5$, $b = 2$, $h_0 = u = 3$, $v = 0.25$, and $w = k = r = 1$ within the interval $-10 \leq x, t \leq 10$ with the 2D profile plotted at $t = 0.1$. Figure 3 depicts an anti-bell-shaped soliton obtained from (3.22) for $a = b = u = 1$, $h_0 = k = r = 0.5$, and $h_1 = v = 0.25$ in the region $-5 \leq x, t \leq 5$, with the 2D outline shown at $t = 0.5$. Figure 4 presents a bright soliton for solution (3.23) evaluated at $a = 3.25$, $b = k = 1$, $h_0 = 0.75$, $h_1 = u = v = 0.25$, and $r = 0.3$ within $-5 \leq x, t \leq 5$, while the 2D graph is extracted at $t = 0.1$ for the interval $-10 \leq x, t \leq 10$. Figure 5 characterizes a localized W-shaped soliton derived from (3.27) with $a = h_1 = 5$, $b = h_0 = 0.5$, $u = r = 1$, $v = 3$, $w = 2$, and $k = -0.5$ in $-5 \leq x, t \leq 5$, with the 2D plot illustrated at $t = -0.5$. Figure 6 is an anti-bell-shaped soliton corresponding to (3.30) for $a = 4$, $b = -1$, $h_0 = M = 2$, $h_1 = 3$ and $k = r = 1$ and during $-5 \leq x, t \leq 5$, with 2D sketches displayed at $t = 0.5$. Figure 7 demonstrates a W-shaped soliton from (3.31) under for $a = r = M = 1$, $b = -1$, $h_0 = 2$, and $h_1 = 3$ within $-2 \leq x, t \leq 2$, whereas the 2D profile is represented at $t = -0.1$ the range $-5 \leq x, t \leq 5$. Figure 8 portrays a bright soliton obtained from (3.33) using $a = 3.5$, $b = h_1 = w = k = r = 1$, $h_0 = 2$, and $v = 2.5$ within $-5 \leq x, t \leq 5$, labelled at $t = 0.1$ for the 2D profile. Figure 9 features an anti-kink soliton from (3.34) for $a = u = 3$, $b = 0.25$, $h_0 = h_1 = v = n = 2$, and $k = r = m = 1$ within $-5 \leq x, t \leq 5$, with 2D outlines depicted at $t = 0.1$. Figure 10 exhibits a kink soliton based on (3.35) under $a = v = h_0 = 0.75$, $b = h_1 = m = 0.25$, $u = n = k = 3$, and $r = 2$ in the interval $-5 \leq x, t \leq 5$, with the 2D plot described at $t = 0.5$.

Furthermore, the graphical representations presented in Figures 11–16 illustrate the diverse physical profiles of the exact soliton solutions systematically derived via the improved method: Figure 11 demonstrates an anti-bell-shaped soliton from solution (3.41) for $a = b = c = 2$, and $k = r = 1$, with 2D plots sketched at $t = 0.1$. Figure 12 reveals a bright soliton from (3.42) under $a = b = c = 2$, and $k = r = 1$ in $-5 \le x, t \le 5$, with 2D sketches captured at $t = 0.1$. Figure 13 displays a periodic wave structure from (3.43) obtained for $a = b = c = 2$, $k = 1$, and $r = -2$ in the range $-5 \le x, t \le 5$, with 2D figures plotted at $t = 0.01$ within $-10 \le x, t \le 10$. Figure 14 illustrates an anti-bell-shaped soliton derived from (3.49) for $a = 0.5$, $b = k = 1$, $c = g_0 = 3$, and $h_1 = r = 2$ within $-5 \le x, t \le 5$, with 2D graphs illustrated at $t = 0.01$ in the interval $-10 \le x, t \le 10$. Figure 15 depicts a W-shaped soliton for solution (3.50) under $a = 0.5$, $b = k = 1$, $c = g_0 = 3$, and $h_1 = r = 2$ in $-5 \le x, t \le 5$, while 2D outlines are described at $t = 0.01$ in $-10 \le x, t \le 10$. Figure 16 confirms a periodic soliton structure from (3.55) evaluated for $a = 0.5$, $b = g_0 = 1$, $c = k = 2$, $h_1 = 5$, and $r = -3$ within $-5 \le x, t \le 5$, with 2D sketches exhibited at $t = 0.1$.

These results demonstrate the structural diversity and wave dynamics of the cKGZ system. Transitions among localized, singular, and periodic waveforms, driven by parameter variations, confirm the impact of nonlinear dispersion on wave propagation and energy localization within plasmas. In these figures, the 2D cross-sectional profiles are plotted for multiple values of the wave speed c to demonstrate its specific influence on wave amplitude and spatial localization.

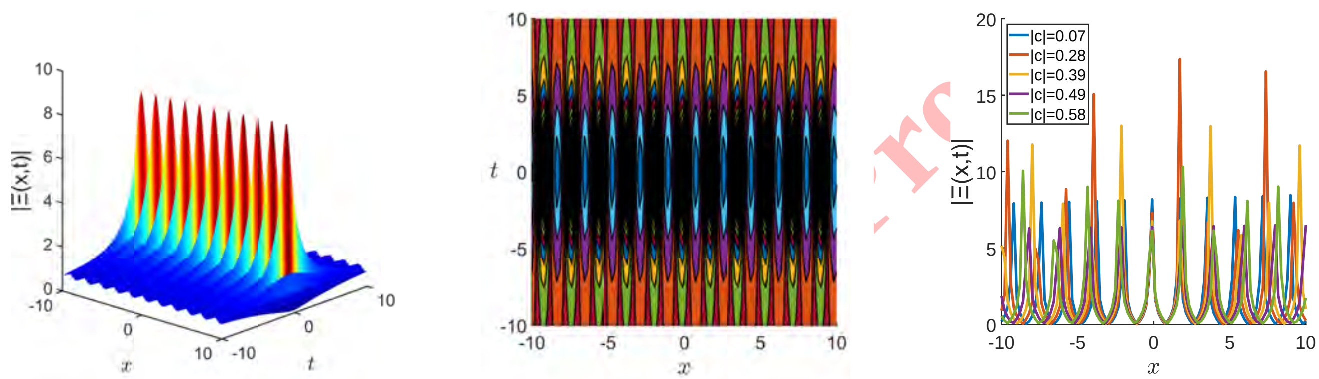

(A) 3D. (B) Contour. (C) 2D.

FIGURE 2. Singular periodic soliton of (3.18) for $a = h_1 = 5$, $b = 2$, $h_0 = u = 3$, $v = 0.25$, $w = k = r = 1$.

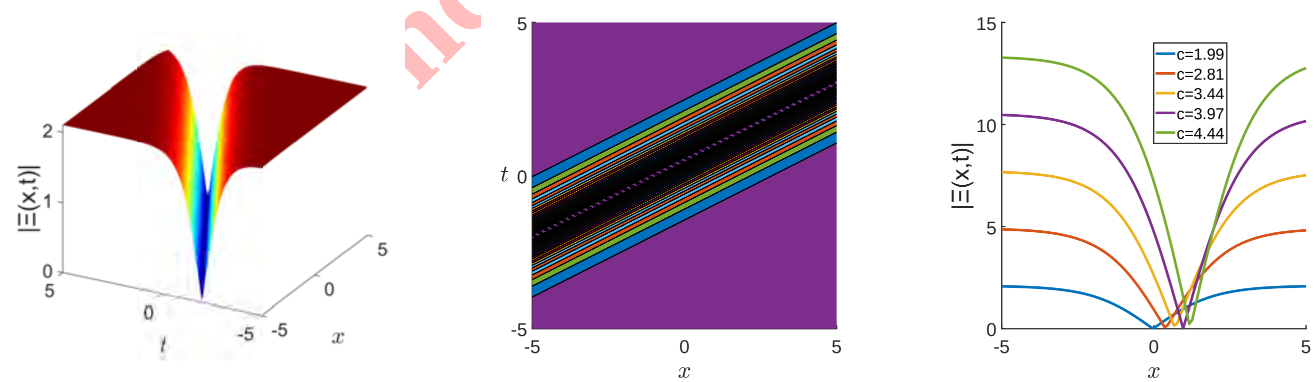

(A) 3D. (B) Contour. (C) 2D.

FIGURE 3. Anti-bell-shaped soliton of (3.22) for $a = b = u = 1$, $h_0 = k = r = 0.5$, and $h_1 = v = 0.25$.

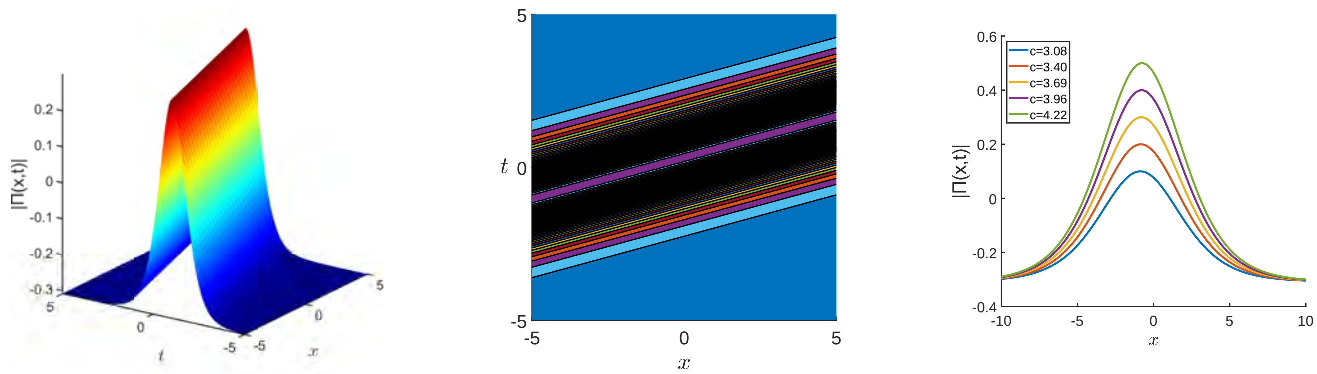

(A) 3D. (B) Contour. (C) 2D.

FIGURE 4. Bright soliton of (3.23) for $a = 3.25$, $b = k = 1$, $h_0 = 0.75$, $h_1 = u = v = 0.25$, and $r = 0.3$.

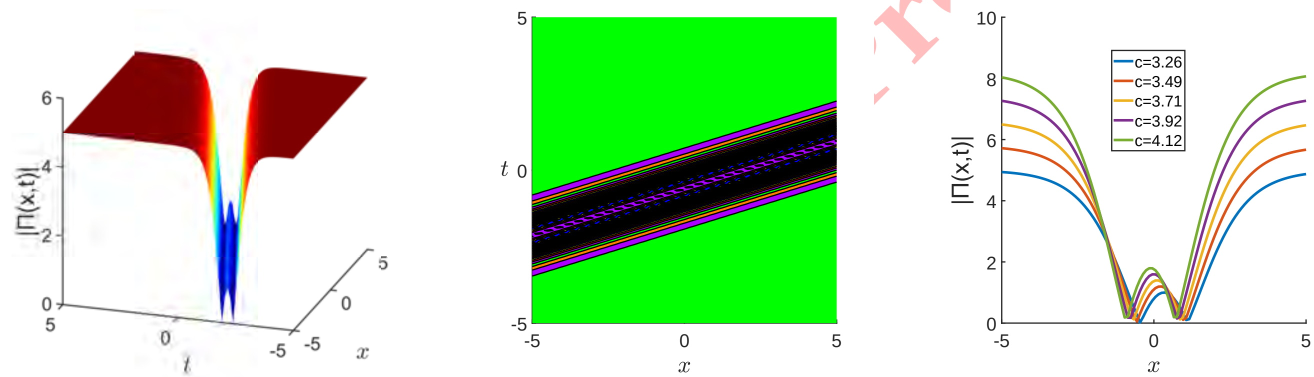

(A) 3D. (B) Contour. (C) 2D.

FIGURE 5. Localized W-shaped soliton of (3.27) for $a = h_1 = 5$, $b = h_0 = 0.5$, $u = r = 1$, $v = 3$, $w = 2$, and $k = -0.5$.

5. Numerical simulation and verification

To verify the analytical solutions, the cKGZ model is numerically integrated using the finite difference method (FDM) coupled with an ODE solver, selecting the exact W-shaped soliton from solution (3.31) as the test case. Figure 17(a) illustrates the numerical time evolution of this profile from $t = 0$ to $t = 1$, where the continuous surface confirms stable propagation without dispersive radiation. Furthermore, a 2D cross-sectional comparison at $t = 1$ (Figure 17(b)) validates close agreement between the exact (solid line) and numerical (dashed line) profiles. Finally, the absolute error, plotted in Figure 17(c), remains bounded at an order of 10^{-4}, verifying the accuracy and reliability of the derived analytical formulations.

6. Bifurcation analysis

The bifurcation analysis of the dynamical system associated with the nonlinear cKGZ equation provides valuable insights into the qualitative behavior of its solutions. NLPDEs can be effectively analyzed through dynamical system approaches [5, 28, 33], which allow the study of stability, equilibrium states, and transition behaviors. The trajectories

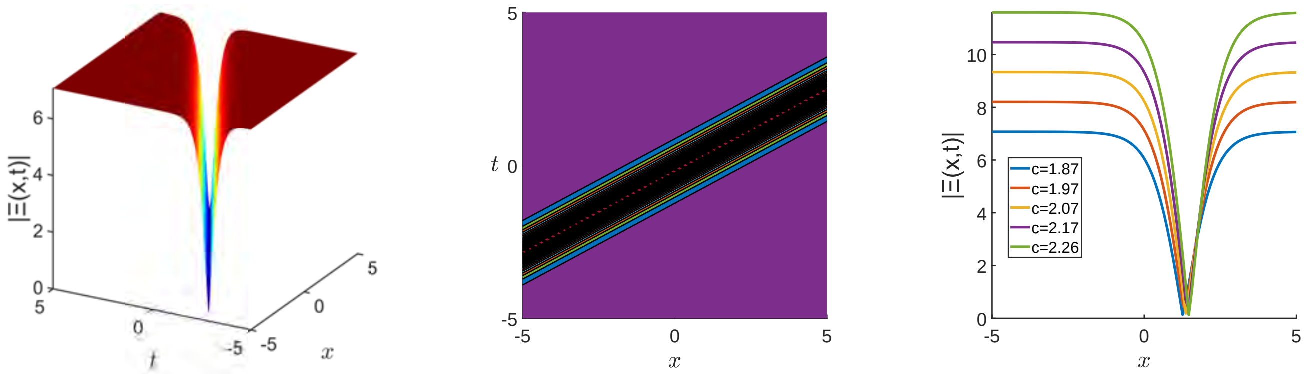

(A) 3D. (B) Contour. (C) 2D.

FIGURE 6. Anti-bell-shaped soliton of (3.30) for $a = 4$, $b = -1$, $h_0 = M = 2$, $h_1 = 3$, and $k = r = 1$.

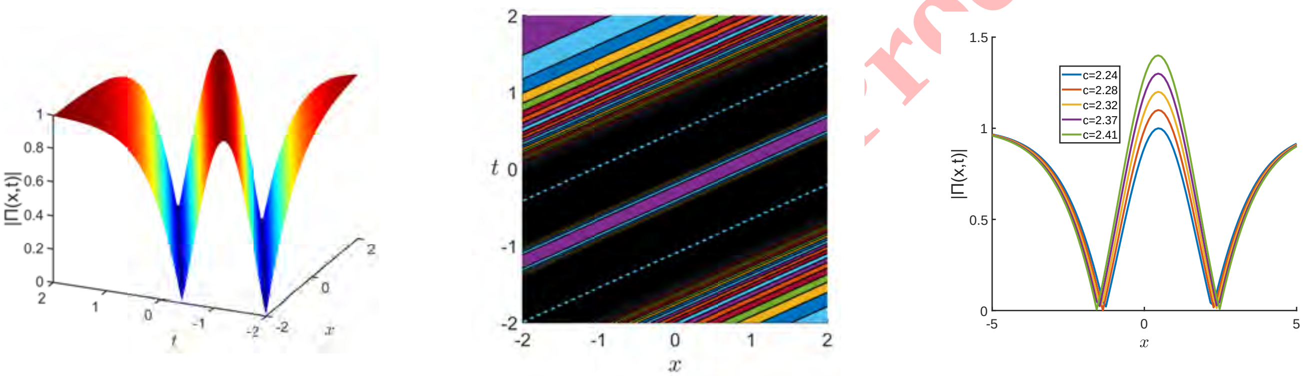

(A) 3D. (B) Contour. (C) 2D.

FIGURE 7. W-shaped soliton of (3.31) for $a = r = M = 1$, $b = -1$, $h_0 = 2$, and $h_1 = 3$.

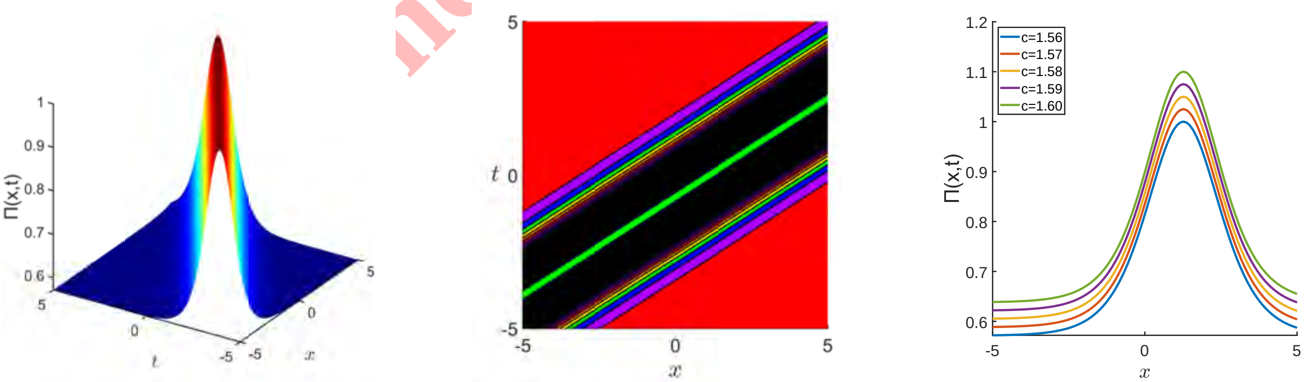

(A) 3D. (B) Contour. (C) 2D.

FIGURE 8. Bright soliton of (3.33) for $a = 3.5$, $b = h_1 = w = k = r = 1$, $h_0 = 2$, and $v = 2.5$.

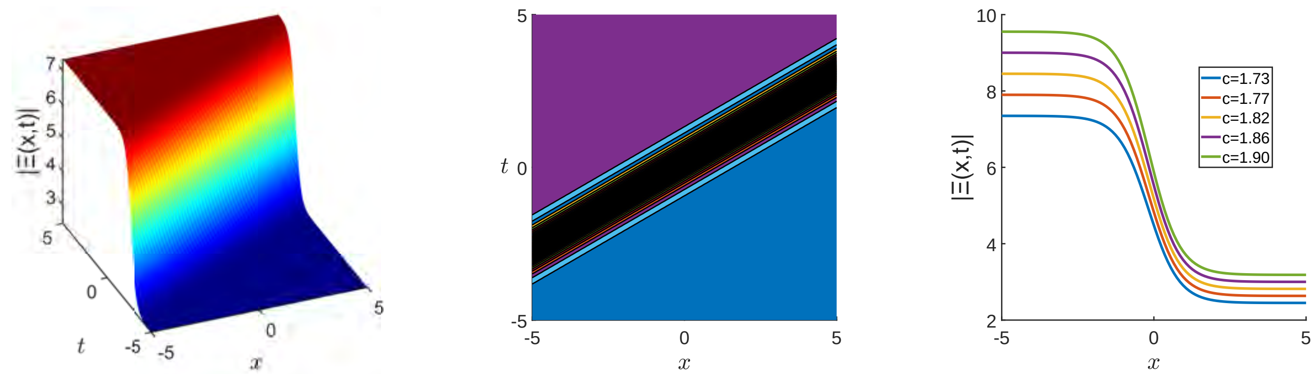

(A) 3D. (B) Contour. (C) 2D.

FIGURE 9. Anti-kink soliton of (3.34) for $a = u = 3$, $b = 0.25$, $h_0 = h_1 = v = n = 2$, and $k = r = m = 1$.

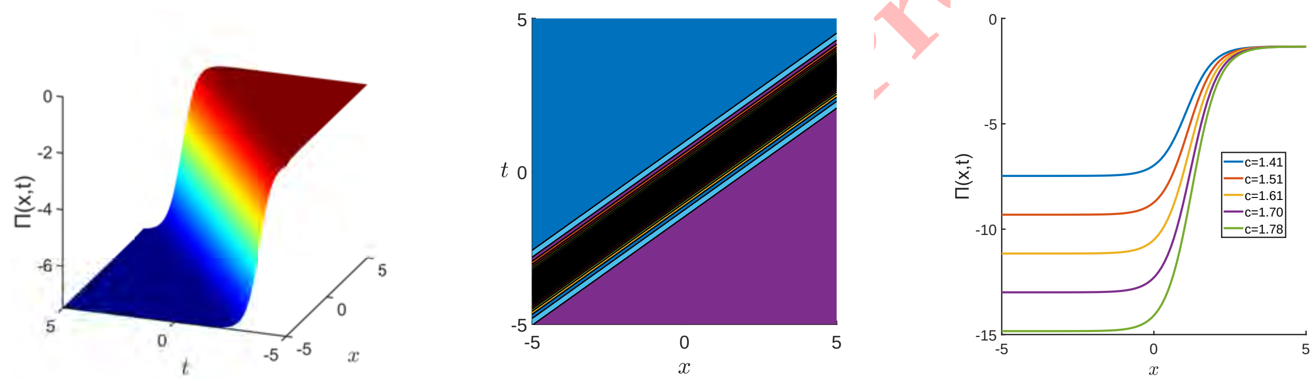

(A) 3D. (B) Contour. (C) 2D.

FIGURE 10. Kink soliton of (3.35) for $a = v = h_0 = 0.75$, $b = h_1 = m = 0.25$, $u = n = k = 3$, and $r = 2$.

of the associated dynamical structure can be displayed as simple closed curves, fixed points, or other topologically equivalent orbits. Variations of the free parameters can significantly affect the physical configuration of the system by changing equilibrium points, modifying stability properties, and inducing bifurcations. Such analysis increases the understanding of the nonlinear dynamics of cKGZ systems and helps to predict transitions between different wave modes and identify regions of stable and unstable behavior.

6.1. **The phase plane analysis.** In this section, we analyze the phase plane of the cKGZ model. It helps to classify the system's behaviors like nodes, saddles, or spirals and analyze nonlinear dynamics intuitively and graphically.

Setting $P = M$ and $M' = N$, Eq. (3.14) can be expressed in the form of a first-order dynamical system as follows:

$$\begin{aligned} \frac{dM}{d\sigma} &= N, \\ \frac{dN}{d\sigma} &= -s_1 M - s_2 M^3. \end{aligned} \tag{6.1}$$

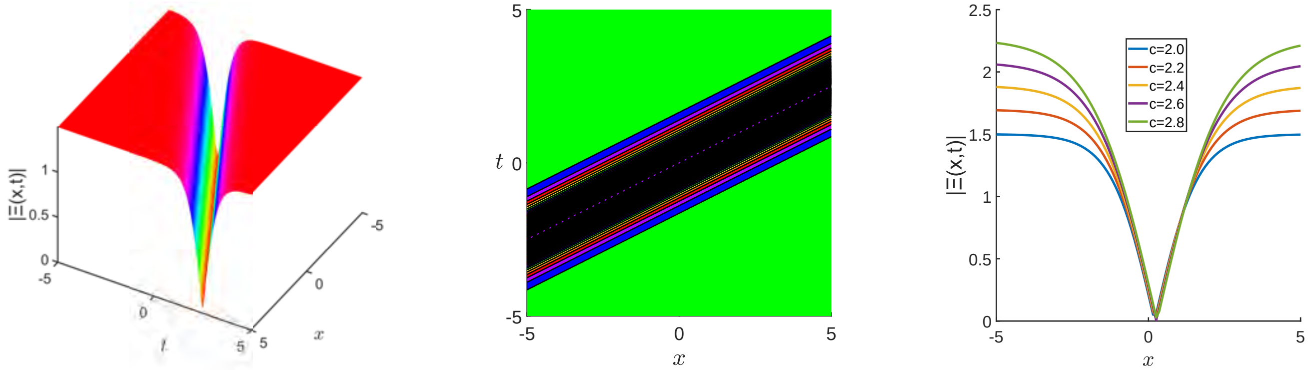

(A) 3D. (B) Contour. (C) 2D.

FIGURE 11. Anti-bell-shaped soliton of (3.41) for $a = b = c = 2$, and $k = r = 1$.

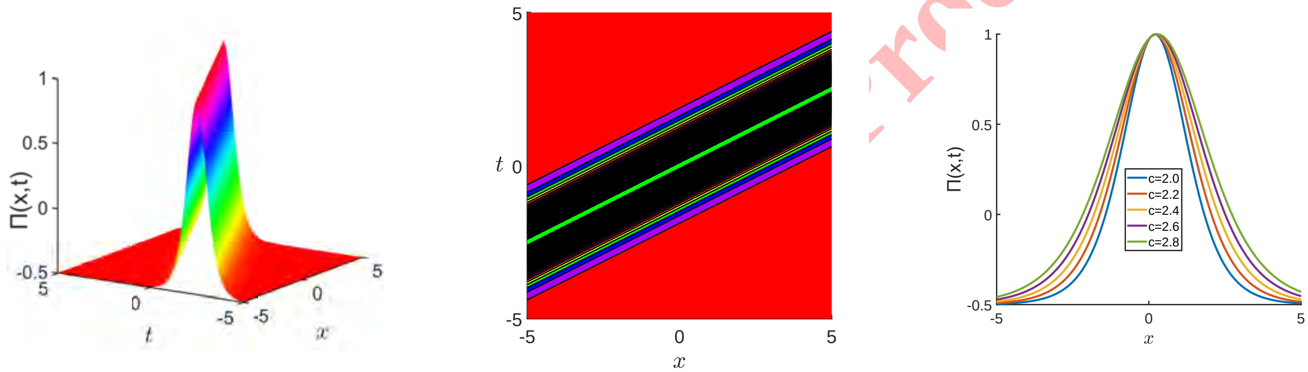

(A) 3D. (B) Contour. (C) 2D.

FIGURE 12. Bright soliton of (3.42) for $a = b = c = 2$, and $k = r = 1$.

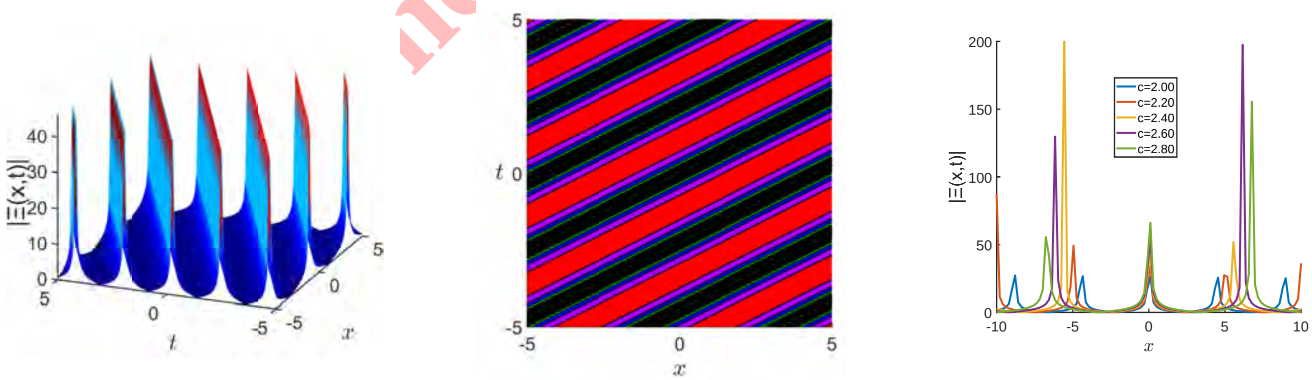

(A) 3D. (B) Contour. (C) 2D.

FIGURE 13. Periodic wave structure of (3.43) for $a = b = c = 2$, $k = 1$, and $r = -2$.

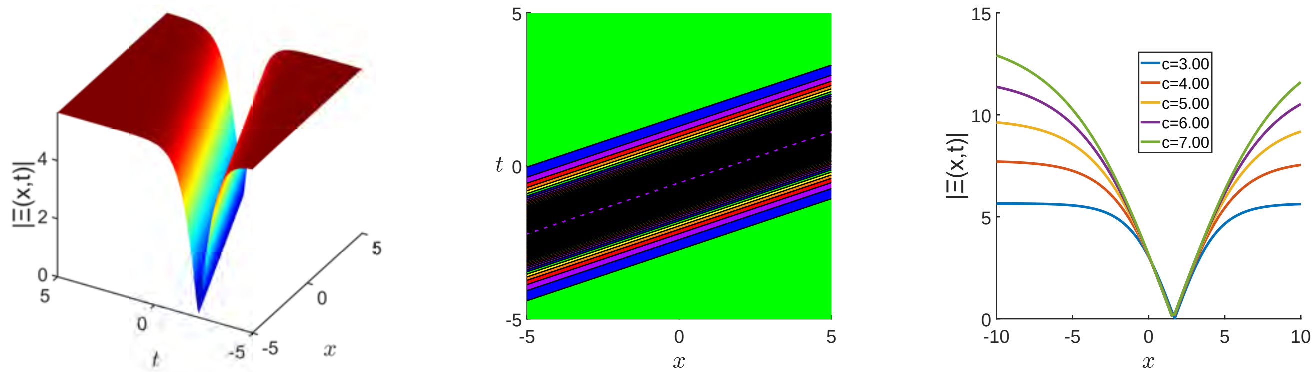

(A) 3D. (B) Contour. (C) 2D.

FIGURE 14. Anti-bell-shaped soliton of (3.49) for $a = 0.5$, $b = k = 1$, $c = g_0 = 3$, and $h_1 = r = 2$.

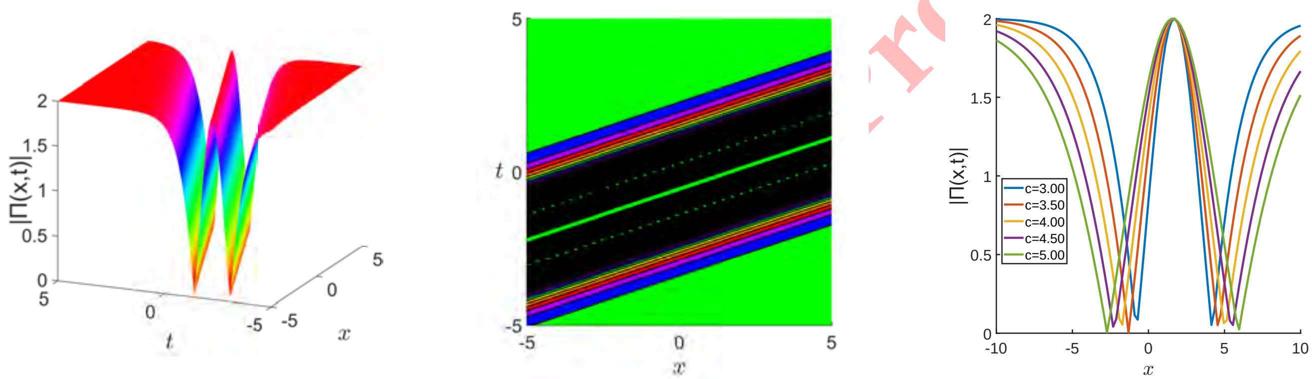

(A) 3D. (B) Contour. (C) 2D.

FIGURE 15. W-shaped soliton of (3.50) for $a = 0.5$, $b = k = 1$, $c = g_0 = 3$, and $h_1 = r = 2$.

The Hamiltonian function associated with the planar system (6.1) is:

$$H(M,N) = \frac{1}{2}N^2 + \frac{1}{2}s_1 M^2 + \frac{1}{4}s_2 M^4 = h, \tag{6.2}$$

where $s_1 = \frac{1+ar}{k^2(c-1)}$, $s_2 = \frac{2ab}{k^2(c-1)^2}$, and H is the Hamiltonian function.

The equilibrium points of Eq. (6.1) are found by putting $M' = 0$ and $N' = 0$, on the basis of the dynamical principle of differential equations. As a result, we attain one equilibrium point as $E_1(M,N) = (0,0)$ when $s_1 s_2 > 0$. We found three equilibrium points when $s_1 s_2 < 0$, namely $E_1(M,N) = (0,0)$ and $E_{2,3}(M,N) = \left(\pm\sqrt{-\frac{s_1}{s_2}}, 0\right)$.

The determinant form of the Jacobian matrix of the dynamical system (6.1) is as follows:

$$J(M,N) = \begin{vmatrix} 0 & 1 \\ -s_1 - 3s_2 M^2 & 0 \end{vmatrix} = s_1 + 3s_2 M^2. \tag{6.3}$$

The characteristics value of the Jacobian matrix is $\pm\sqrt{-s_1 - 3s_2 M^2}$ at the position (M,N). At any equilibrium point $E(M,N)$, the postulate $J(M,N) > 0$ ensures that the point is a center point, $J(M,N) < 0$ confirms a saddle point and $J(M,N) = 0$ is for a cuspidal point.

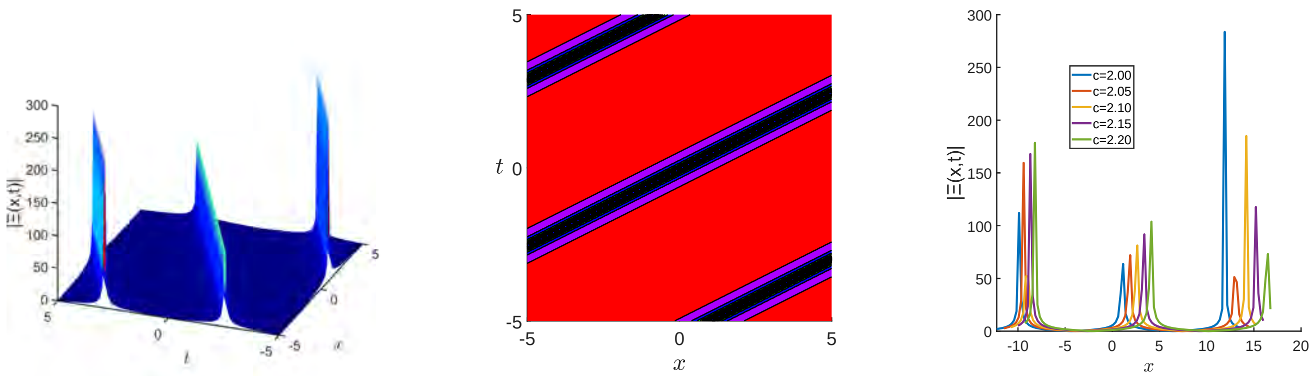

(A) 3D. (B) Contour. (C) 2D.

FIGURE 16. Periodic soliton structure of (3.55) for $a = 0.5$, $b = g_0 = 1$, $c = k = 2$, $h_1 = 5$, and $r = -3$.

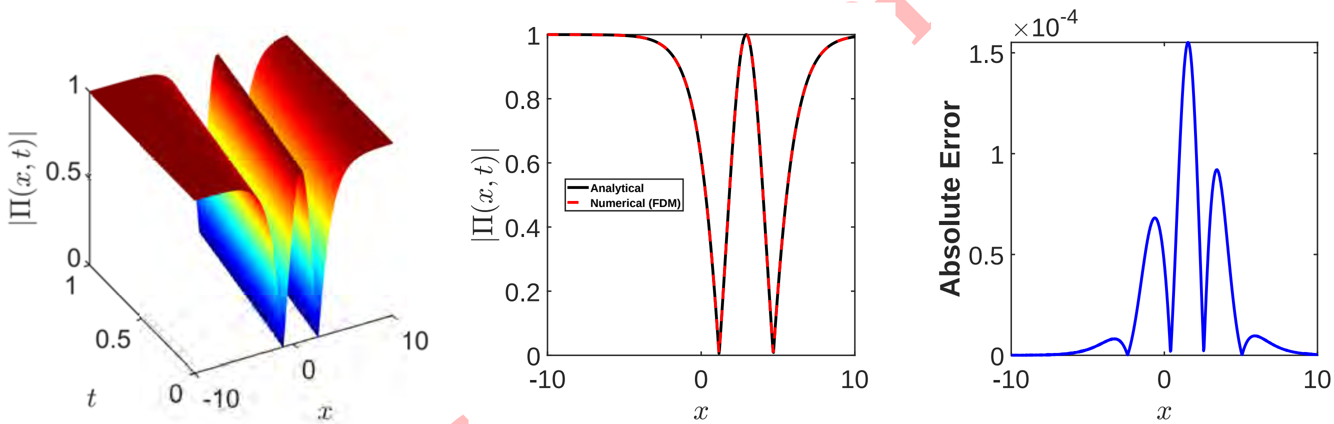

(A) 3D numerical solution. (B) 2D comparison. (C) Absolute errors.

FIGURE 17. Numerical validation of the W-shaped soliton of (3.31): (A) 3D spatiotemporal evolution; (B) 2D comparison of exact and FDM solutions at $t = 1$; (C) Absolute error profile.

Case 1: For $s_1 > 0$ and $s_2 > 0$

Taking the value of the parameters as $a = b = k = r = 1$ and $c = 3$, we found one equilibrium point $E_1(0, 0)$ fixing a center as shown in Figure 18. We observe that it encompasses only one cluster of periodic orbits acquiring from Eq. (6.1).

Case 2: For $s_1 < 0$ and $s_2 < 0$

By choosing the numerical value of the arbitrary constants as $a = k = r = 1$ and $b = c = -1$, we acquire one equilibrium point $E_1(0, 0)$ representing a saddle point as displayed in Figure 19, which stands for non-closed trajectories.

Case 3: For $s_1 < 0$ and $s_2 > 0$

For $a = b = k = r = 1$ and $c = -1$, we obtain $E_1(0,0)$ and $E_{2,3}(\pm\sqrt{2},0)$ as equilibrium points displayed in Figure 20, where E_1 represents a saddle point and $E_{2,3}$ are center points. The trajectories comprise closed curves surrounding diverse solutions such as periodic (blue), homoclinic orbits (red) and hyper periodic (green).

Case 4: For $s_1 > 0$ and $s_2 < 0$

With the value of the parameters $a = k = r = 1$, $b = -1$ and $c = 2$, we found three equilibrium points $E_1(0,0)$ and $E_{2,3}(\pm 1,0)$ shown in Figure 21, whereas E_1 represents a center point and $E_{2,3}$ represent saddle points and it confirmed the presence of kink and anti-kink solitons via the relationship of two heteroclinic orbits $E_2(1,0)$ and $E_3(-1,0)$.

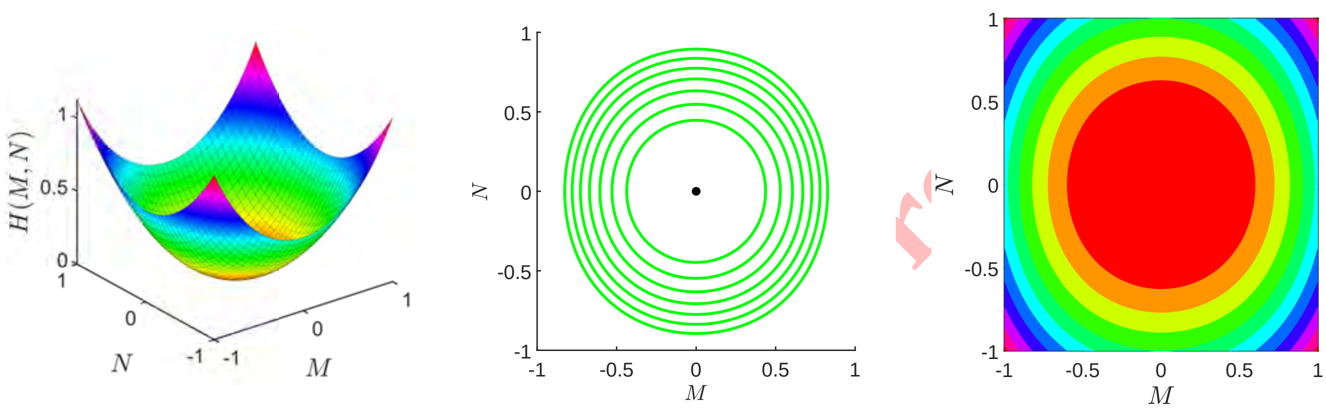

(A) 3D. (B) Contour plot. (C) Phase portrait.

FIGURE 18. For the conditions $s_1 > 0$ and $s_2 > 0$, the phase portrait with the equilibrium $E(0,0)$ of (6.1) for $a = b = k = r = 1$ and $c = 3$.

6.2. **Potential energy function.** The potential function is associated with the dynamical system. With the help of the potential energy function, we can clearly describe the behavior of the dynamic system of the considered model. Mainly, the function describes the potential energy of the system, whereas the Hamiltonian function describes the entire energy of Eq. (6.1). The relation (6.2) is a first integral of the dynamic system (6.1) and can be viewed as the energy of a particle with an effective potential as:

$$V(M) = \frac{1}{2}s_1 M^2 + \frac{1}{4}s_2 M^4, \tag{6.4}$$

where $s_1 = \frac{1+ar}{k^2(c-1)}$ and $s_2 = \frac{2ab}{k^2(c-1)^2}$.

In Figure 22, we show the potential energy under different conditions as discussed in subsection 6.1. This helps us better understand the behavior of the dynamical system in the study.

6.3. **Chaotic behavior analysis.** Chaotic analysis describes the behaviors of a chaotic system over time with very small changes in the initial conditions. We can observe vast changes over time due to minor deviations in the initial conditions or tiny variations in the perturbation term. The perturbation term $\theta\cos(\omega t)$ is introduced into Eq. (6.1)

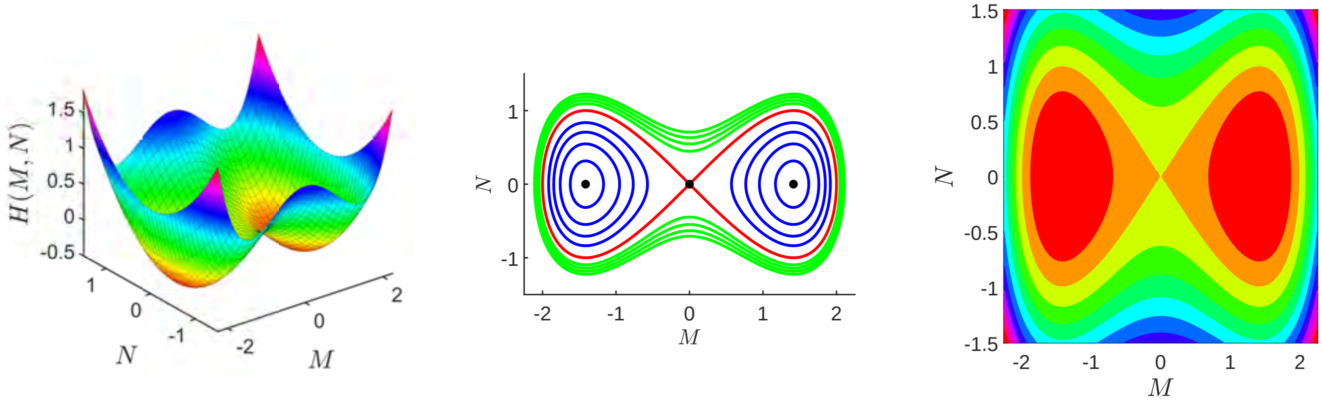

(A) 3D. (B) Contour plot. (C) Phase portrait.

FIGURE 19. The phase portrait of the equilibrium point $E(0,0)$ of (6.1) under the assumption $s_1 < 0$, $s_2 < 0$ with $a = k = r = 1$ and $b = c = -1$.

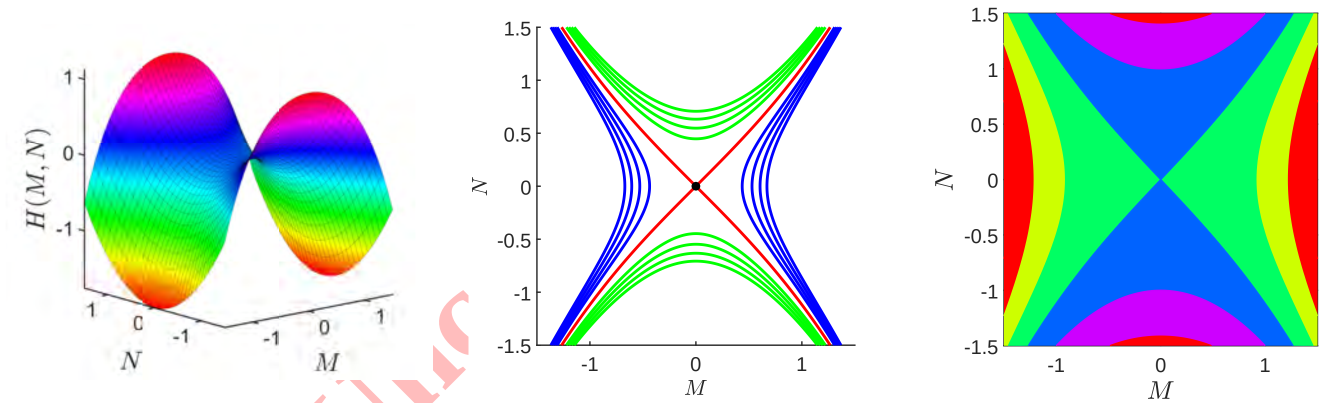

(A) 3D. (B) Contour plot. (C) Phase portrait.

FIGURE 20. Phase portrait with the condition $s_1 < 0$, $s_2 > 0$, equilibrium points $E_1(0,0)$ and $E_{2,3}(\pm\sqrt{2},0)$ of (6.1) for $a = b = k = r = 1$ and $c = -1$.

as follows:

$$\frac{dM}{d\sigma} = N,$$
$$\frac{dN}{d\sigma} = -s_1 M - s_2 M^3 + \theta\cos(\omega t), \tag{6.5}$$

where θ represents the amplitude and ω is the frequency of the system. By using Eq. (6.5), we can understand the chaotic behavior of the cKGZ model. Subsequently, the chaotic character of Eq. (6.5) is figured out for numerous

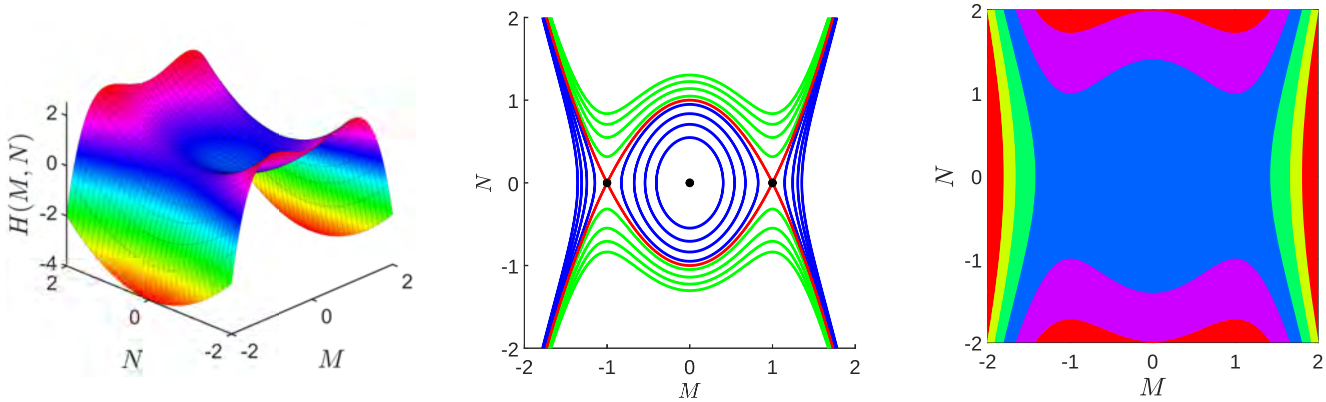

(A) 3D. (B) Contour plot. (C) Phase portrait.

FIGURE 21. For (6.1) with $a = k = r = 1$, $b = -1$ and $c = 2$ provides the phase portrait for equilibrium point $E_1(0,0)$ and $E_{2,3}(\pm 1, 0)$ under $s_1 > 0$, $s_2 < 0$.

particular values of the free parameters with various initial conditions. For better representation, we depict the chaotic dynamics in 3D and 2D for Case 1 ($s_1 > 0$, $s_2 > 0$) and Case 3 ($s_1 < 0$, $s_2 > 0$) of section 6.1 in Figures. 23 and 24, respectively.

6.4. **Sensitivity analysis.** In this section, the sensitive behavior of Eq. (6.5) is analyzed in a wide sense. We consider the same conditions $s_1 > 0$ and $s_2 > 0$ alongside the fixed values $a = b = k = r = 1$ and $c = 3$ as stated in Case 1 of section 6.1. We also illustrate the sensitive behavior for Eq. (6.5) for various amplitudes and frequencies with different initial values in Figure 25. Figure 26 depicts sensitive behavior for different values of frequency and amplitude with several initial conditions and the fixed parameters $a = b = k = r = 1$ and $c = -1$, with the assumptions $s_1 < 0$ and $s_2 > 0$ as maintained in Case 3 of section 6.1, to highlight the changes clearly.

For better graphical representation and understanding, we maintain the same numerical values for some of the parameters throughout the bifurcation analysis based on the conditions. The initial conditions are the same for the chaotic behavior analysis and time series analysis (or sensitivity analysis). However, for better visualization, we sketch the time series plot by taking the time from 0 to 100, whereas we use the time duration 0 to 500 in the chaotic analysis.

7. MODULATION INSTABILITY

In this portion, we establish the modulation instability of the governing cKGZ model, given in Eq. (1.1) and Eq. (1.2), which is observed as localized high-density regions in plasma waves and refers to the amplification of small perturbations in a continuous wave or steady-state solution due to the interplay between nonlinearity and dispersion. Now, consider the perturbed solution of the subsequent type [4]:

$$p(x,t) = H_0 + \delta W(x,t). \tag{7.1}$$

Then we can write the solutions as:

$$\Xi(x,t) = (1+i)(H_0 + \delta W(x,t)), \tag{7.2}$$

$$\Pi(x,t) = r + \frac{2b(H_0 + \delta W(x,t))^2}{c^2 - 1}, \tag{7.3}$$

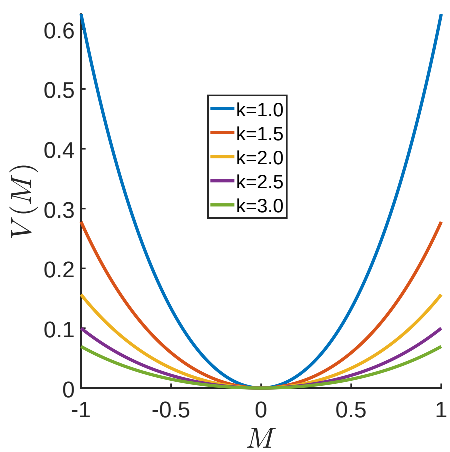

(A) $s_1 > 0, s_2 > 0$.

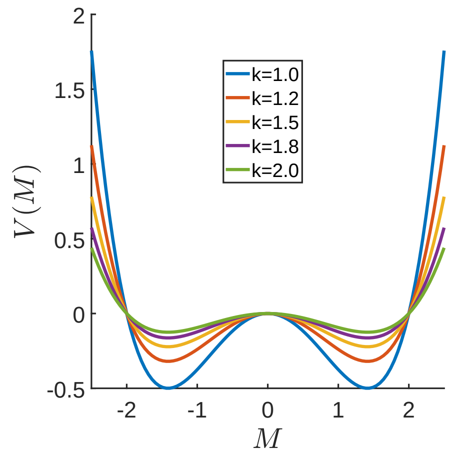

(B) $s_1 < 0, s_2 < 0$.

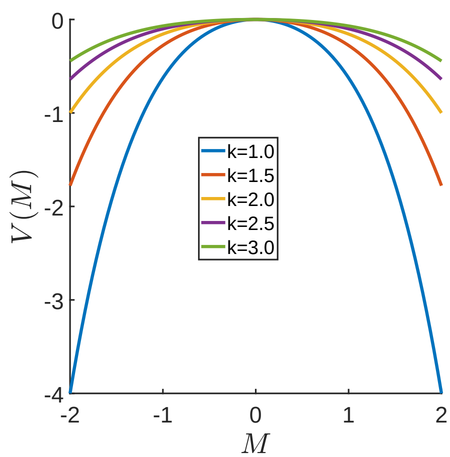

(C) $s_1 < 0, s_2 > 0$.

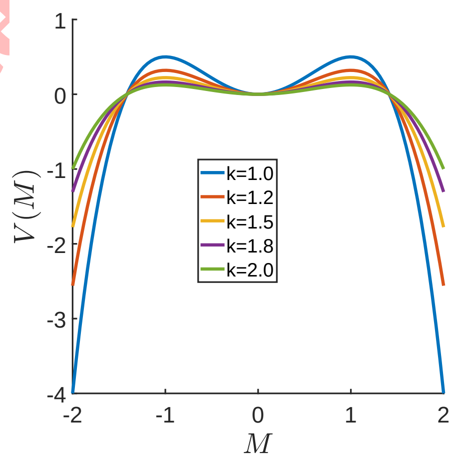

(D) $s_1 > 0, s_2 < 0$.

Figure 22. The effective potential energy of (6.2) with the various conditions.

where H_0 represents the steady-state solution, $\delta \ll 1$, and $W(x,t)$ is an unknown function. Using Eq. (7.2) and Eq. (7.3) in our considered model Eq. (1.1) and Eq. (1.2) and linearizing with respect to δ, we get:

$$ar\delta W + \frac{6abH_0^2\delta W}{c^2-1} + arH_0 + \frac{2abH_0^3}{c^2-1} + \delta W + H_0 + \delta W_{tt} - \delta W_{xx} = 0, \tag{7.4}$$

$$-2H_0b\delta W_x + \frac{4H_0b\delta W_{tt}}{c^2-1} - \frac{4H_0b\delta W_{xx}}{c^2-1} = 0. \quad)$$

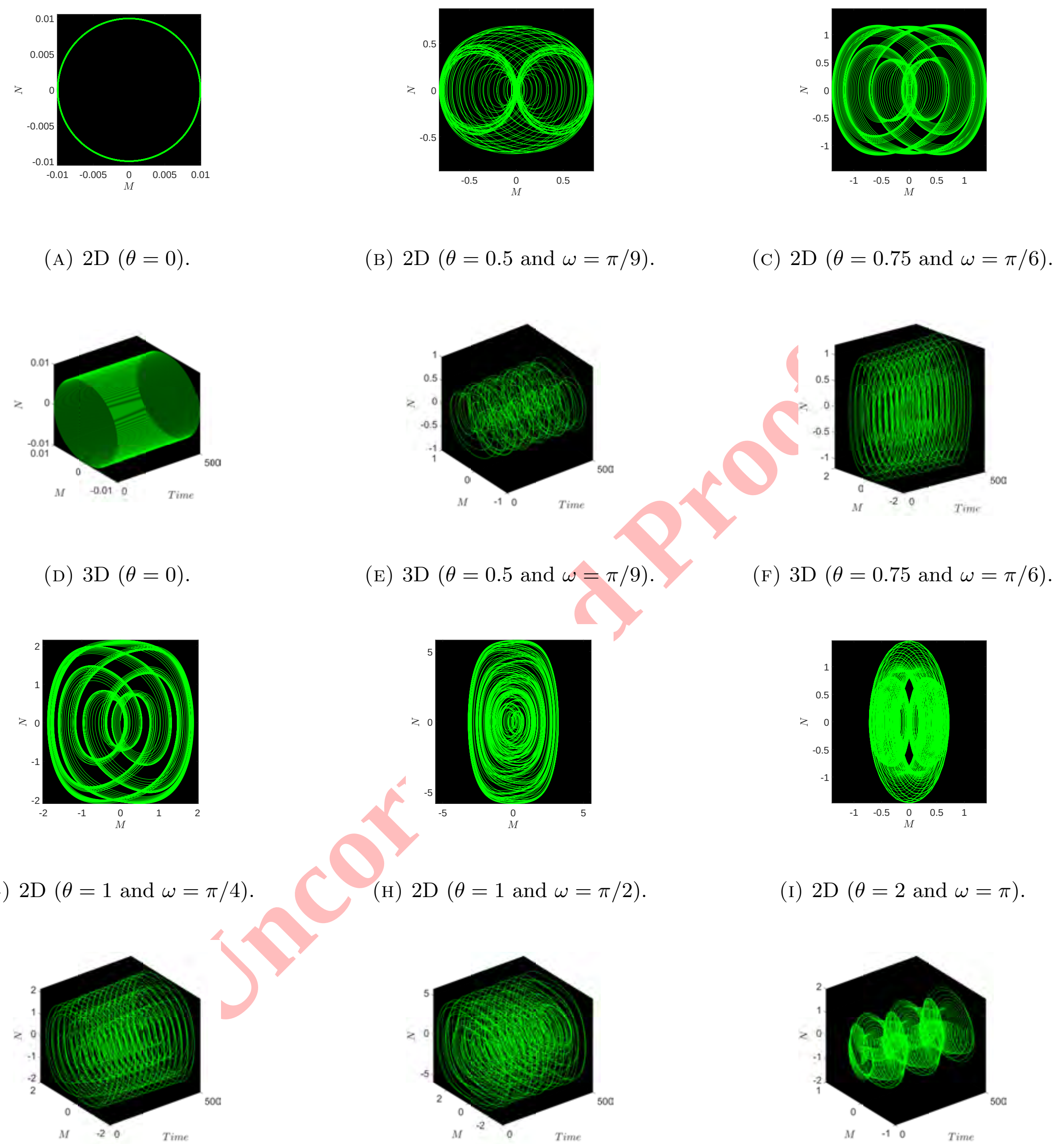

(A) 2D ($\theta = 0$). (B) 2D ($\theta = 0.5$ and $\omega = \pi/9$). (C) 2D ($\theta = 0.75$ and $\omega = \pi/6$).

(D) 3D ($\theta = 0$). (E) 3D ($\theta = 0.5$ and $\omega = \pi/9$). (F) 3D ($\theta = 0.75$ and $\omega = \pi/6$).

(G) 2D ($\theta = 1$ and $\omega = \pi/4$). (H) 2D ($\theta = 1$ and $\omega = \pi/2$). (I) 2D ($\theta = 2$ and $\omega = \pi$).

(J) 3D ($\theta = 1$ and $\omega = \pi/4$). (K) 3D ($\theta = 1$ and $\omega = \pi/2$). (L) 3D ($\theta = 2$ and $\omega = \pi$).

FIGURE 23. For (6.4) with $a = b = k = r = 1$, $c = 3$ and various values of θ and ω give diverse chaotic figures.

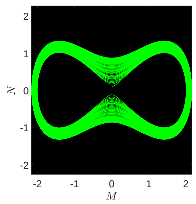

(A) 2D ($\theta = 0$).

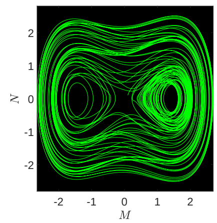

(B) 2D ($\theta = 0.25$ and $\omega = \pi/4$).

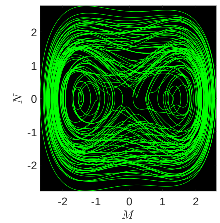

(C) 2D ($\theta = 0.5$ and $\omega = \pi/2$).

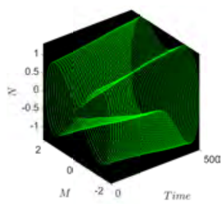

(D) 3D ($\theta = 0$).

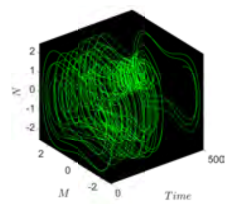

(E) 3D ($\theta = 0.25$ and $\omega = \pi/4$).

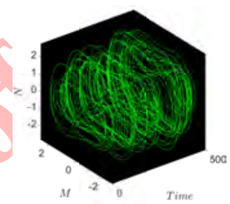

(F) 3D ($\theta = 0.5$ and $\omega = \pi/2$).

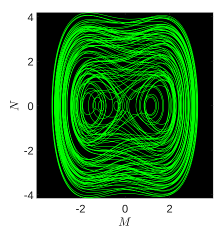

(G) 2D ($\theta = 0.75$ and $\omega = \pi/3$).

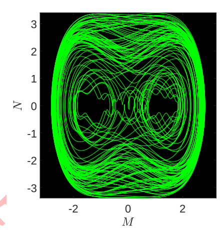

(H) 2D ($\theta = 1$ and $\omega = \pi$).

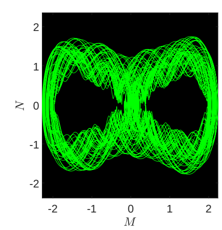

(I) 2D ($\theta = 2$ and $\omega = 2\pi$).

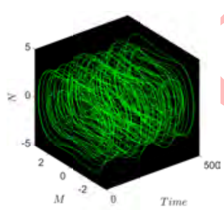

(J) 3D ($\theta = 0.75$ and $\omega = \pi/3$).

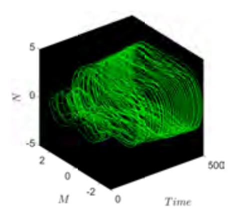

(K) 3D ($\theta = 1$ and $\omega = \pi$).

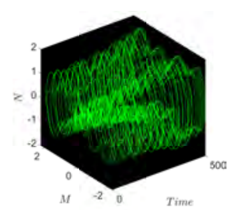

(L) 3D ($\theta = 2$ and $\omega = 2\pi$).

FIGURE 24. Various chaotic graphs of (6.4) for $a = b = k = r = 1$, $c = -1$ and different values of θ and ω.

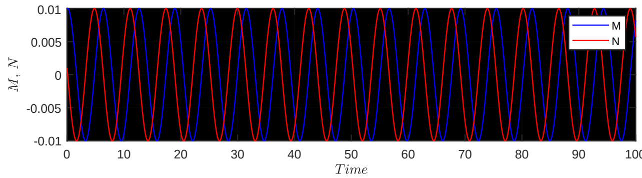

(A) Initial conditions $(0.01, 0.001)$ with $\theta = 0$.

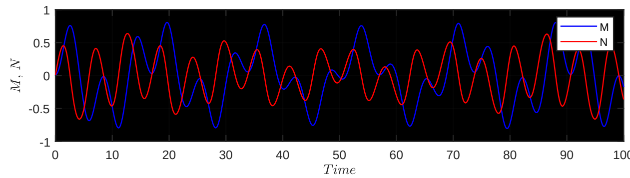

(B) Initial conditions $(0.01, 0.01)$ with $\theta = 0.5$ & $\omega = \pi/9$.

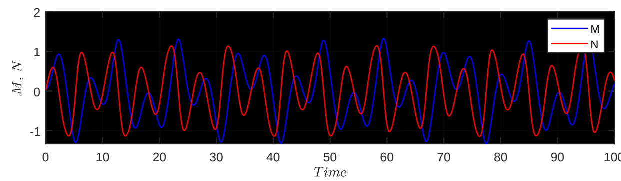

(C) Initial conditions $(0.05, 0.025)$ with $\theta = 0.75$ & $\omega = \pi/6$.

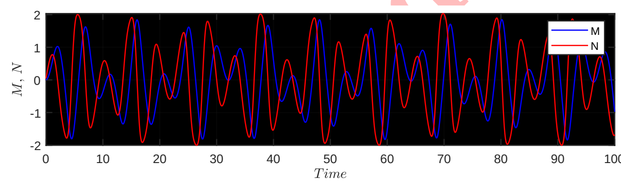

(D) Initial conditions $(0.001, 0.05)$ with $\theta = 1$ & $\omega = \pi/4$.

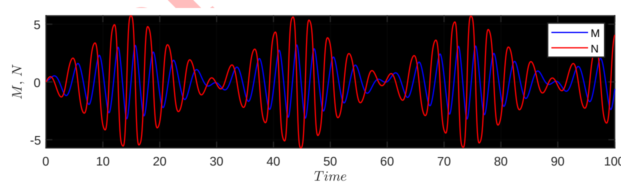

(E) Initial conditions $(0.1, 0.001)$ with $\theta = 1$ & $\omega = \pi/2$.

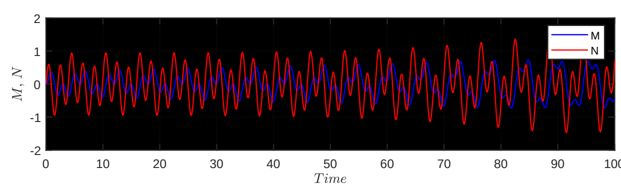

(F) Initial conditions $(0.001, 0.001)$ with $\theta = 2$ & $\omega = \pi$.

FIGURE 25. Time series of (6.5) for $a = b = k = r = 1$, $c = 3$ and various values of θ, ω and distinct initial conditions.

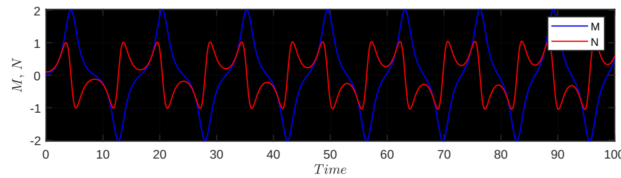

(A) Initial conditions $(0, 0.1)$ with $\theta = 0$.

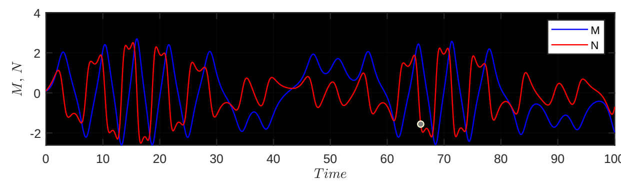

(B) Initial conditions $(0.1, 0.1)$ with $\theta = 0.25$ & $\omega = \pi/4$.

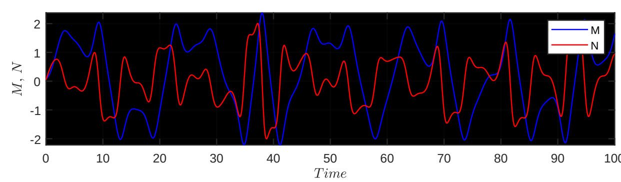

(C) Initial conditions $(0.1, 0.05)$ with $\theta = 0.5$ & $\omega = \pi/2$.

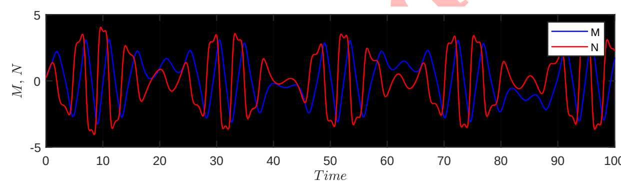

(D) Initial conditions $(0.5, 0.25)$ with $\theta = 0.75$ & $\omega = \pi/3$.

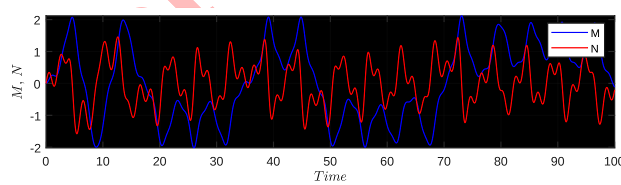

(E) Initial conditions $(0.01, 0)$ with $\theta = 1$ & $\omega = \pi$.

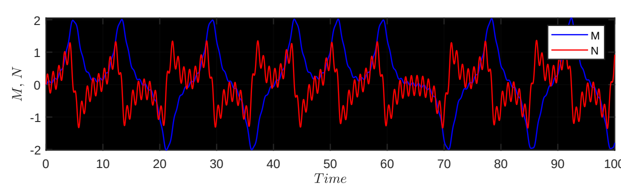

(F) Initial conditions $(0.01, 0.001)$ with $\theta = 2$ & $\omega = 2\pi$.

FIGURE 26. Time series figure for (6.5) with $a = b = k = r = 1$, $c = -1$, different values of θ, ω and various initial conditions.

Now, consider the solution for the unknown function as:

$$W(x,t) = e^{i(kx+\mu t)}, \tag{7.6}$$

where k is the normalized wave number and μ represents the frequency. Substituting the solution into Eq. (7.4) and Eq. (7.5), we get:

$$are^{i(kx+\mu t)} + \frac{6abH_0^2 e^{i(kx+\mu t)}}{c^2-1} + e^{i(kx+\mu t)} - \mu^2 e^{i(kx+\mu t)} + k^2 e^{i(kx+\mu t)} = 0, \tag{7.7}$$

$$-ike^{i(kx+\mu t)}(c^2-1) - 2\mu^2 e^{i(kx+\mu t)} + 2k^2 e^{i(kx+\mu t)} = 0. \tag{7.8}$$

Simplifying, we attain:

$$ar + \frac{6abH_0^2}{c^2-1} + 1 - \mu^2 + k^2 = 0, \tag{7.9}$$

$$-ik(c^2-1) - 2\mu^2 + 2k^2 = 0. \tag{7.10}$$

We can rewrite Eq. (7.10) as:

$$(c^2-1) = \frac{2k^2 - 2\mu^2}{ik}. \tag{7.11}$$

Now, using Eq. (7.11) and Eq. (7.9), we obtain:

$$ar + \frac{6iabkH_0^2}{2(k^2-\mu^2)} + 1 - \mu^2 + k^2 = 0. \tag{7.12}$$

Solving Eq. (7.12) for μ, we find:

$$\mu = \pm\frac{1}{\sqrt{2}}\sqrt{1 + ar + 2k^2 \pm \sqrt{(1 + 2ar + a^2r^2 - 12iabkH_0^2)}}. \tag{7.13}$$

It is evident from Eq. (7.13) that the governing Eq. (1.1) and Eq. (1.2) are stable and unstable under the various conditions detailed in Table 2.

TABLE 2. Stability conditions for the wave propagation.

State	**Condition**
Stable	$\mathrm{Re}(\mu) > 0, \quad \mathrm{Re}(\mu) < 0, \quad \mathrm{Im}(\mu) > 0$
Unstable	$\mathrm{Im}(\mu) < 0$
Marginal Stable	$\mu = 0$

In Figure 27, we sketch the modulation instability for the different values of μ. The propagation is marginally stable (red line) when $\mu = 0$. If μ is a real number, or if $\mathrm{Im}(\mu) > 0$, then the propagation is stable. Whereas, the propagation becomes unstable when μ has a negative imaginary part ($\mathrm{Im}(\mu) < 0$).

7.1. **Computational stability verification.** To visualize the impact of modulation instability on the exact solutions obtained, we perform a numerical simulation by superimposing a small harmonic perturbation on the steady-state W-shaped soliton from the solution Eq. (3.31). The perturbed wave profile at any given time t is obtained by computing the real part of the perturbation from Eq. (7.6):

$$|\Pi_{\text{perturbed}}| = |\Pi_{\text{exact}}| + \epsilon e^{-\mathrm{Im}(\mu)t}\cos(kx + \mathrm{Re}(\mu)t), \tag{7.14}$$

where ϵ represents the initial noise amplitude (perturbation parameter), k is the spatial wave number of the noise, and μ is the modulation frequency. Figure 28 plots the evolution of the perturbed soliton at $t = 1$. These results are consistent with the theoretical stability criteria. Specifically, for purely real frequencies ($\mu = 4, -4$) and zero

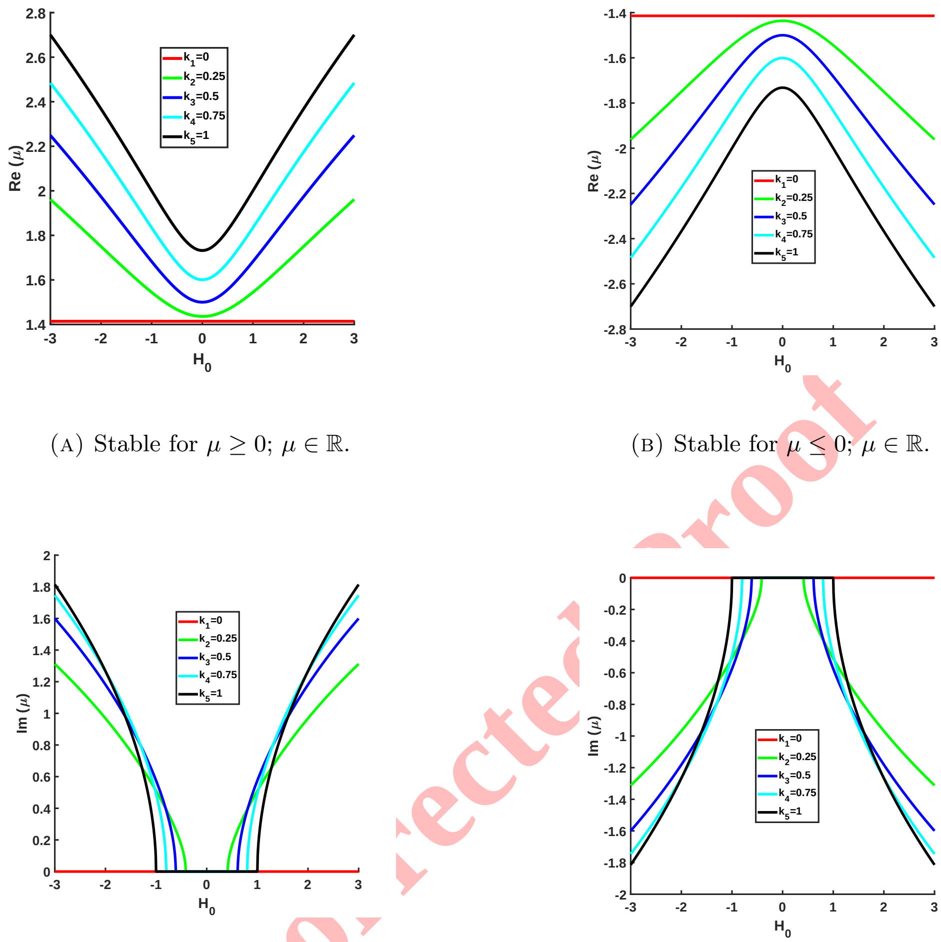

(A) Stable for $\mu \geq 0$; $\mu \in \mathbb{R}$.

(B) Stable for $\mu \leq 0$; $\mu \in \mathbb{R}$.

(C) Stable for $\mu \geq 0$; $\mu \in \mathbb{C}$.

(D) Unstable for $\mu \leq 0$; $\mu \in \mathbb{C}$.

FIGURE 27. Modulation instability plots of (7.13) for $a = r = 1$ and $b = \sqrt{-1}$.

frequency ($\mu = 0$), the growth factor $e^{-\mathrm{Im}(\mu)t}$ remains 1. In these cases, the perturbation oscillates as a bounded harmonic wave across the soliton, thereby preserving its structural stability. Furthermore, for a positive imaginary frequency ($\mu = 2i$), the factor $e^{-\mathrm{Im}(\mu)t}$ exponentially decays to zero, restoring the exact soliton profile. In contrast, for a negative imaginary frequency ($\mu = -2i$), the exponent becomes positive, leading to an exponential growth of the perturbation. As observed in Figure 28, this unstable regime distorts the localized W-shaped structure. This computational verification demonstrates that the derived exact solutions satisfy the physical conditions of modulation instability.

8. Conclusions

The mathematical analysis of the cKGZ system provides a comprehensive understanding of high-frequency electric field oscillations and low-frequency ion-acoustic wave dynamics and interactions. The improved auxiliary equation and

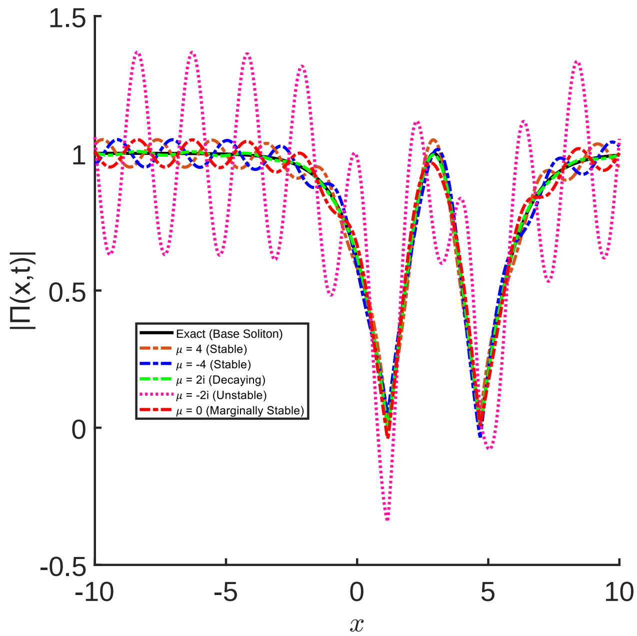

FIGURE 28. Impact of varying modulation frequencies (μ) on the W-shaped soliton at $t = 1$. The wave keeps stability for $Im(\mu) \geq 0$, whereas a negative imaginary frequency ($Im(\mu) < 0$) triggers rapid structural breakdown.

improved tanh methods yield diverse exact solutions, including localized W-shaped, rational, singular, bright, dark, kink, anti-kink, bell, anti-bell, and periodic profiles. Additionally, 2D multi-plot projections confirm the sensitivity of wave amplitude and spatial localization to the wave speed c. Through bifurcation theory, this study identifies key equilibrium points, such as centers and saddles, that determine the system's stability structure and transition pathways between different dynamical regimes. The inclusion of external perturbations reveals the onset of quasi-periodic and chaotic behaviors, emphasizing the balance between nonlinearity and dispersion inherent in the system. Furthermore, the physical significance of this research is demonstrated by formulating the modulation instability criteria to assess the stability of steady-state regimes, which is verified through numerical simulations. From a mathematical physics perspective, the results bridge nonlinear differential equations and dynamical systems theory to describe realistic plasma processes. This framework enhances the predictive capability of analytical plasma models and can be extended to explore related nonlinear systems in optics, fluid dynamics, and condensed matter physics. This study advances the theoretical foundation for analyzing and controlling nonlinear wave phenomena in complex physical media.

CRediT authorship contribution statement

Tobibur Rahman: Conceptualization, Software, Methodology, Investigation, Visualization, Writing - original draft, Writing - review & editing.

Md. Tarikul Islam: Supervision, Funding acquisition, Conceptualization, Data curation, Writing - review & editing.

M. Ali Akbar: Formal analysis, Validation, Resources, Project administration, Supervision, Writing - review & editing.

Appendix A

A.1. Parameter sets for the improved auxiliary equation scheme. Case II:

$$g_0 = \pm\frac{vh_0(ar+1)}{k(4uw-v^2)\sqrt{-ab}}, \quad g_1 = \pm\frac{2wh_0(ar+1)}{k(4uw-v^2)\sqrt{-ab}}, \quad h_1 = 0,$$
$$c = \mp\frac{\sqrt{k^2(4uw-v^2)-2(ar+1)}}{k\sqrt{4uw-v^2}}.$$

Case III:

$$g_0 = \mp\frac{(ar+1)h_0}{kv\sqrt{-ab}}, \quad g_1 = 0, \quad h_1 = \frac{2wh_0}{v}, \quad c = \mp\frac{\sqrt{k^2(4uw-v^2)-2(ar+1)}}{k\sqrt{4uw-v^2}}.$$

A.2. Parameter sets for the improved tanh technique. Case III:

$$e_0 = 0, \quad e_1 = \pm\frac{g_0\sqrt{(ar+1)(c^2-1)}}{2\sqrt{2ab\phi}}, \quad f_1 = \mp\frac{g_0\sqrt{\phi(ar+1)(c^2-1)}}{2\sqrt{2ab}}, \quad g_1 = h_1 = 0,$$
$$k = \pm\frac{\sqrt{-(ar+1)}}{2\sqrt{2\phi(c^2-1)}}.$$

Case IV:

$$e_0 = 0, \quad e_1 = \pm\frac{g_0\sqrt{(ar+1)(c^2-1)}}{\sqrt{2ab\phi}}, \quad f_1 = g_1 = h_1 = 0, \quad k = \pm\frac{\sqrt{-(ar+1)}}{\sqrt{2\phi(c^2-1)}}.$$

Case V:

$$e_0 = 0, \quad e_1 = \pm\frac{g_0\sqrt{-(ar+1)(c^2-1)}}{2\sqrt{ab\phi}}, \quad f_1 = \mp\frac{g_0\sqrt{\phi(ar+1)(c^2-1)}}{2\sqrt{-ab}}, \quad g_1 = h_1 = 0,$$
$$k = \pm\frac{\sqrt{ar+1}}{2\sqrt{\phi(c^2-1)}}.$$

Case VI:

$$e_0 = \mp\frac{h_1k(c^2-1)}{\sqrt{-ab}}, \quad e_1 = \mp\frac{kg_0(c^2-1)}{\sqrt{-ab}}, \quad f_1 = g_1 = 0, \quad \phi = -\frac{ar+1}{2k^2(c^2-1)}.$$

References

[1] M. A. E. Abdelrahman, and G. Alshreef, *Closed-form solutions to the new coupled Konno-Oono equation and the Kaup-Newell model equation in magnetic field with novel statistic application*, Eur. Phys. J. Plus, *136* (2021), 455.

[2] M. J. Ablowitz and H. Segur, *Solitons and the inverse scattering transform*, Soc. Indus. Appl. Math., 1981.

[3] A. Akbulut and F. Taşcan, *Application of conservation theorem and modified extended tanh-function method to (1+1)-dimensional nonlinear coupled Klein-Gordon-Zakharov equation*, Chaos, Solitons & Fractals, *104* (2017), 33–40.

[4] F. Badshah, K. U. Tariq, H. Ilyas, and R. N. Tufail, *Soliton, lumps, stability analysis and modulation instability for an extended (2+1)-dimensional Boussinesq model in shallow water*, Chaos, Solitons & Fractals, *187* (2024), 115352.

[5] B. Barnes and G. R. Fulford, *Mathematical modelling with case studies: a differential equations approach using Maple and MATLAB*, CRC Press, 2011.

[6] H. M. Baskonus, T. A. Sulaiman, and H. Bulut, *On the new wave behavior to the Klein-Gordon-Zakharov equations in plasma physics*, Indian J. Phys., *93* (2019), 393–399.

[7] S. Carillo and O. Ragnisco, *Nonlinear evolution equations and dynamical systems*, Springer Sci. Business Media, 2012.
[8] L. A. Dawod, M. Lakestani, and J. Manafian, *Breather wave solutions for the (3+1)-d generalized shallow water wave equation with variable coefficients*, Qual. Theory Dyn. Syst., *22* (2023), 127.
[9] R. O. Dendy, *Plasma Dynamics*, Oxford University Press, Oxford, 1990.
[10] A. A. Gaber, A. F. Aljohani, A. Ebaid, and J. T. Machado, *The generalized Kudryashov method for nonlinear space-time fractional partial differential equations of Burgers type*, Nonlin. Dyn., *95* (2019), 361–368.
[11] M. G. Hafez and M. A. Akbar, *New exact traveling wave solutions to the (1+1)-dimensional Klein-Gordon-Zakharov equation for wave propagation in plasma using the exp-expansion method*, Propulsion Power Res., *4* (2015), 31–39.
[12] S. Hakkaev, M. Stanislavova, and A. Stefanov, *Orbital stability for periodic standing waves of the Klein-Gordon-Zakharov system and the beam equation*, Z. Angew. Math. Phys., *64* (2013), 265–282.
[13] R. Hirota, *The direct method in soliton theory*, Cambridge Univ. Press, 2004.
[14] A. Houwe, S. Abbagari, Y. Salathiel, M. Inc, S. Y. Doka, K. T. Crépin, and D. Baleanu, *Complex traveling-wave and solitons solutions to the Klein-Gordon Zakharov equations*, Results Phys., *17* (2020), 103127.
[15] M. T. Islam, H. Alsaud, T. Rahman, and M. Inc, *Exclusive soliton solutions arise in mono-mode optical fibre connecting to nonlinear Fokas system*, Opt. Quant. Electron., *56* (2024), 753.
[16] M. T. Islam, M. A. Aktar, J. F. G. Aguilar, and J. T. Jimenez, *Further innovative optical solitons of fractional nonlinear quadratic-cubic Schrödinger equation via two techniques*, Opt. Quant. Electron., *53* (2021), 562.
[17] M. T. Islam, T. Rahman, M. Inc, and M. A. Akbar, *Comprehensive soliton solutions of fractional stochastic Kraenkel-Manna-Merle equations in ferromagnetic materials*, Opt. Quant. Electron., *56* (2024), 927.
[18] M. T. Islam, M. A. Akbar, J. F. G. Aguilar, E. Bonyah, and G. F. Anaya, *Assorted soliton structures of solutions for fractional nonlinear Schrodinger types evolution equations*, J. Ocean Eng. Sci., *7* (2022), 528–535.
[19] M. T. Islam, S. Ryehan, F. A. Abdullah, and J. F. G. Aguilar, *The effect of Brownian motion and noise strength on solutions of stochastic Bogoyavlenskii model alongside conformable fractional derivative*, Optik, *287* (2023), 171140.
[20] M. M. A. Khater, A. A. Mousa, M. A. El-Shorbagy, and R. A. M. Attia, *Abundant novel wave solutions of nonlinear Klein-Gordon-Zakharov (KGZ) model*, Eur. Phys. J. Plus, *136* (2021), 1–11.
[21] M. M. A. Khater, *On the dynamics of strong Langmuir turbulence through the five recent numerical schemes in the plasma physics*, Numer. Methods Partial Differ. Eq., *38* (2022), 719–728.
[22] M. Lakestani and J. Manafian, *Analytical treatments of the space-time fractional coupled nonlinear Schrödinger equations*, Opt. Quant. Electron., *50* (2018), 396.
[23] B. Q. Li and Y. L. Ma, *Oscillation rogue waves for the Kraenkel-Manna-Merle in ferrites*, J. Magn. Magn. Mater., *537* (2021), 168182.
[24] Q. Li, X. Zheng, and Z. Wang, *Orbital stability of periodic standing waves of the coupled Klein-Gordon-Zakharov equations*, AIMS Math., *8* (2023), 8560–8579.
[25] S. Liu, Z. Fu, S. Liu, and Q. Zhao, *Jacobi elliptic function expansion method and periodic wave solutions of nonlinear wave equations*, Phys. Lett. A, *289* (2001), 69–74.
[26] Y. L. Ma and B. Q. Li, *Kraenkel-Manna-Merle saturated ferromagnetic system: Darboux transformation and loop-like soliton excitations*, Chaos, Solitons & Fractals, *159* (2022), 112179.
[27] I. E. Mhlanga and C. M. Khalique, *Exact solutions of the symmetric regularized long wave equation and the Klein-Gordon-Zakharov equations*, Abstr. Appl. Anal., *2014* (2014), 679016.
[28] M. M. Miah, F. Alsharif, M. A. Iqbal, J. R. M. Borhan, and M. Kanan, *Chaotic phenomena, sensitivity analysis, bifurcation analysis, and new abundant solitary wave structures of the two nonlinear dynamical models in industrial optimization*, Mathematics, *12* (2024), 1959.
[29] W. W. Mohammed, F. M. Al-Askar, and C. Cesarano, *The analytical solutions of the stochastic mKdV equation via the mapping method*, Mathematics, *10* (2022), 4212.
[30] S. Nestor, A. Houwe, H. Rezazadeh, A. Bekir, G. Betchewe, and S. Y. Doka, *New solitary waves for the Klein-Gordon-Zakharov equations*, Mod. Phys. Lett. B, *34* (2020), 2050246.

[31] Y. Qian, J. Manafian, S. Y. Mohyaldeen, L. S. Esmail, S. A. Gorovoy, and G. Singh, *Multiple-order line rogue wave, lump and its interaction, periodic, and cross-kink solutions for the generalized CHKP equation*, Propulsion Power Res., *10* (2021), 277–293.
[32] H. U. Rehman, M. I. Asjad, M. Inc, and I. Iqbal, *Exact solutions for new coupled Konno-Oono equation via Sardar subequation method*, Opt. Quant. Electron., *54* (2022), 798.
[33] M. Sagib, M. A. Hossain, B. K. Saha, and K. Khan, *On traveling wave solutions with stability and phase plane analysis for the modified Benjamin-Bona-Mahony equation*, PLoS One, *19*(7) (2024), e0306196.
[34] M. Shakeel, S. T. Mohyud-Din, and M. A. Iqbal, *Modified extended exp-function method for a system of nonlinear partial differential equations defined by seismic sea waves*, Pramana-J. Phys., *91* (2018), 1–8.
[35] Y. Shang, Y. Huang, and W. Yuan, *New exact traveling wave solutions for the Klein-Gordon-Zakharov equations*, Comput. Math. Appl., *56* (2008), 1441–1450.
[36] Q. Shi, Q. Xiao, and X. Liu, *Extended wave solutions for a nonlinear Klein-Gordon-Zakharov system*, Appl. Math. Comput., *218* (2012), 9922–9929.
[37] K. U. Tariq, J. Manafian, S. Malmir, R. N. Tufail, O. A. Ilhan, and K. H. Mahmoud, *On the structure of the higher dimensional Date-Jimbo-Kashiwara-Miwa model emerging in water waves*, Discov. Appl. Sci., *7* (2025), 576.
[38] H. Triki and N. Boucerredj, *Soliton solutions of the Klein-Gordon-Zakharov equations with power law nonlinearity*, Appl. Math. Comput., *227* (2014), 341–346.
[39] A. M. Wazwaz, *Partial differential equations: Method and applications*, Taylor and Francis, 2002.
[40] A. M. Wazwaz, *The sine-cosine method for obtaining solutions with compact and noncompact structures*, Appl. Math. Comput., *159* (2004), 559–576.
[41] Y. Xu, J. Manafian, O. A. Ilhan, A. Aghazadeh, A. A. Fattah, K. H. Mahmoud, R. A. Barhe, and W. D. Kadhim, *Conservation law, stability analysis, degenerate lump and traveling wave solutions for (2+1)-dimensional KP-BBM equation*, Qual. Theory Dyn. Syst., *24* (2025), 246.
[42] S. W. Yao, S. M. Zekavatmand, H. Rezazadeh, J. Vahidi, M. B. Ghaemi, and M. Inc, *The solitary wave solutions to the Klein-Gordon-Zakharov equations by extended rational methods*, AIP Adv., *11* (2021), 6.
[43] G. Yel, H. M. Baskonus, and H. Bulut, *Novel archetypes of new coupled Konno-Oono equation by using sine-Gordon expansion method*, Opt. Quant. Electron., *49* (2017), 285.
[44] S. Yin, *Stability and instability of the standing waves for the Klein-Gordon-Zakharov system in one space dimension*, Math. Methods Appl. Sci., *41* (2018), 4428–4447.
[45] Z. Zhang, F. L. Xia, and X. P. Li, *Bifurcation analysis and the travelling wave solutions of the Klein-Gordon-Zakharov equations*, Pramana-J. Phys., *80* (2013), 41–59.
[46] X. Zheng, Y. Shang, and X. Peng, *Orbital stability of solitary waves of the coupled Klein-Gordon-Zakharov equations*, Math. Methods Appl. Sci., *40* (2017), 2623–2633.
[47] P. Zhou, J. Manafian, M. Lakestani, O. A. Ilhan, N. J. Bahador, A. A. Fattah, K. H. Mahmoud, R. Nuray, and N. Nagiyeva, *Analytical evaluations using neural network-based method for wave solutions of combined Kairat-II-X differential equation in fluid mechanics*, Sci. Rep., *16* (2026), 7753.
[48] H. Zhu, J. Manafian, A. H. Hammadi, O. A. Ilhan, M. Lakestani, S. Malmir, and K. H. Mahmoud, *Conservation law, Chupin Liu's theorem and propagation of pulses in optical metamaterials modeled by NLSE with power law nonlinearity*, Sci. Rep., *15* (2025), 21649.